Spectroscopic Characterization of Lignocellulosic Biomass

Mikael Thyrel
Faculty of Forestry
Department of Forest Biomaterials and Technology
Umeå

Doctoral Thesis
Swedish University of Agricultural Sciences
Umeå 2014

Acta Universitatis Agriculturae Sueciae
2014:101

Cover: Synchrotron STXM image of Ca crystal at reed canary grass cell wall.
Scale bars represent 5 µm (left image) and 1 µm (right image).
Photo: Mikael Thyrel, Karina Thånell, Chithra Karunakaran

ISSN 1652-6880
ISBN (print version) 978-91-576-8150-8
ISBN (electronic version) 978-91-576-8151-5

Print: Arkitektkopia, Umeå 2014

Spectroscopic characterization of lignocellulosic biomass

Abstract

This thesis focuses on characterization of organic components and inorganic elements in lignocellulosic biomass. The chosen biomass models were mostly wood from conifers and straw from rhizomatous grasses but also forest-based residues and agro-based plants. X-ray fluorescence (XRF) and near infrared (NIR) spectroscopy are techniques that can potentially be incorporated in a future biorefinery concept, where characterization of the feedstock is crucial due to the heterogeneous nature of biomass.

XRF spectroscopy combined with principal component analysis (PCA) was used to classify a number of different biomass materials. Moreover, partial least squares regression calibration models were developed for several ash elements and ash content with good predictive capabilities. The capability of XRF and NIR spectroscopy to measure ash content in biomass was investigated and it was concluded that XRF spectroscopy was the superior method of the two, especially for measuring contaminated material. If the two techniques were used in conjunction, it was possible to estimate the degree of contamination. In an additional study into the potential for future separation techniques, it was shown that the 2D-NIR technique is useful for classifying wood chips, as well as identifying individual wood chips with high extractive content.

Synchrotron-based X-ray absorption techniques such as X-ray absorption near edge structure (XANES) and scanning transmission X-ray microscopy (STXM) based near edge X-ray absorption fine structure (NEXAFS) spectroscopy were used to study the effect of thermal treatment of lignocellulosic material at 300 to 800 °C and low O_2 partial pressures. PCA modelling of Ca XANES spectra in combination with linear fitting of spectra from reference compounds mainly confirmed the results from calculated theoretical thermodynamic models. The results from STXM C 1s NEXAFS spectroscopy showed that thermal treatment up to 300 °C induced only minor change in plant cell walls and that the major decomposition of the carbon matrix occurred between 300 and 500 °C. Nanomapping of Ca by STXM revealed a size distribution of calcium crystals mainly within the 100 to 200 nm range, which might provide an insight into the volatile behaviour of Ca in combustion processes.

Keywords: wood, grass, XRF, NIR, FT-IR, XANES, STXM, NEXAFS, extractives, thermotreatment, ash elements, calcium

Author's address: Mikael Thyrel, SLU, Department of Forest Biomaterials and Technology,SE-901 83 Umeå, Sweden. *E-mail:* mikael.thyrel@ slu.se

Spektroskopisk karakterisering av växtbiomassa

Sammanfattning

Biomassa uppvisar stor kemisk heterogenitet vilket innebär att dess karakterisering är en hörnsten för styrning och kontroll av användningen i bioraffinaderier och bioenergikombinat. Denna karakterisering av såväl organiska beståndsdelar som oorganiska ämnen i växtbiomassa har studerats med spektroskopiska tekniker inom det nära infraröda (NIR) våglängdsområdet, men främst inom röntgenområdet. De röntgentekniker som användes var spektroskopi med röntgenfluorescens (XRF) och synkrotronbaserad röntgenabsorption vid-nära-kant strukturer (XANES) och vid-nära-kant finstrukturer (NEXAFS) samt skannande transmissionmikroskopi (STXM) ner till nanoskala. Biomassamodeller som använts är träbränslen från barrträd och stråbränslen från rhizomgräs men även avverkningsrester från skog och åker.

Med NIR-baserade bilder av flisbitar på ett transportband kunde bitar med högt innehåll av extraktivämnen identifieras. Detta öppnar möjligheter att sortera ut vedflis för att framställa t.ex. biooljor. Med XRF modellerad med principalkomponentanalys (PCA) var det möjligt att särskilja och klassificera olika biomassamaterial. Dessutom visade kalibreringar konstruerade utifrån XRF-spektra och regression med partiella minstakvadrater (PLS) till referenser på en generellt god prediktiv förmåga för biomassans askhalt och askelement som P, K, Si, Na och Al. Genom att jämföra XRF-signalen från oorganiska element med NIR-signalen som bl.a. avläser de störningar inbäddade askelement orsakar bland materialets organiska bindningar kunde också graden av kontaminering av t.ex. oorganiska ämnen i biomassaprover uppskattas.

Effekten av termisk behandling (300-800 °C) av biomaterial vid låga syretryck studerades med synkrotron XANES, STXM och NEXAFS. De nya data som PCA modellering av calcium (Ca) XANES-spektra genererade i kombination med linjär kombinationsanpassning av spektra från relevanta Ca-föreningar verifierade i huvudsak de teoretiskt beräknade termodynamiska Ca-faserna. Resultaten från STXM och NEXAFS visade att termisk behandling upp till 300 °C hade moderat påverkan på cellväggens kolstruktur medan temperaturer mellan 300 och 500 °C resulterade i tydlig nedbrytning av cellväggens kolmatris. Nanokartering av Ca-kristallstrukturer i växtcellerna visade på en fördelning som var förskjuten mot submikrona kristaller (100 till 200 nm) vilket kan bidra till att förklara det icke-förväntade volatila beteendet Ca visat i förbränningsprocesser. Resultaten illustrerar möjligheter att minska askrelaterade problem vid främst pyrolys, förgasning och förbränning. Sammantaget indikerar de också en väg att i framtiden direkt via spektroskopiska data at-line modellberäkna askämnenas faser för olika termiska processer. Detta ökar potentialen att optimera sådana processer nedströms t.ex. genom lämplig biomassamix.

Författarens adress: Mikael Thyrel, SLU, Instutitionen för skogens biomaterial och teknologi, 901 83 Umeå, Sverige. *E-mail:* mikael.thyrel@ slu.se

Till Frida, Isak och Liv

If you want to find the secrets of the universe, think in terms of energy, frequency and vibration

Nikola Tesla

Contents

List of Publications **9**

Abbreviations **11**

1 Introduction **13**
1.1 Composition of lignocellulosic biomass 14
1.1.1 Ash elements 15
1.2 Thermal treatment of biomass at low oxygen partial pressures 16
1.3 Electromagnetic radiation 19
1.4 Near infrared spectroscopy (NIR) 20
1.5 X-ray fluorescence (XRF) spectroscopy 20
1.5.1 Theory 20
1.5.2 Scatter effects 22
1.5.3 Fluorescence yield 23
1.5.4 Matrix effects 23
1.5.5 XRF calibration 24
1.6 X-ray absorption spectroscopy 25
1.6.1 Synchrotron light 25
1.6.2 Absorption measurements 26
1.6.3 EXAFS 28
1.6.4 XANES 29
1.7 X-ray diffraction (XRD) 30
1.8 Scanning transmission X-ray microscopy (STXM**)** 31
1.9 Multivariate statistics 32
1.9.1 Principal component analysis (PCA) 32
1.9.2 Partial least squares (PLS) regression 33
1.9.3 Diagnostics 35
1.9.4 Multivariate image analysis (MIA) 37
1.10 Objectives 39

2 Material and methods **41**
2.1 Biomaterials and pre-treatments 42
2.2 Analytical methods and instruments 44
2.3 Modelling and software 46

3 Results and discussion **49**
3.1 Characterization of the organic matrix of biomass 49

3.1.1 2-D NIR for separation of wood chips 49
3.1.2 Carbon transformation in thermally treated RCG cell walls. 51
3.2 Characterization of inorganic elements in biomass 54
3.2.1 XRF and NIR characterization of biomass 54
3.2.2 PLS calibration modelling of ash elements and content 55
3.3 X-ray absorption spectroscopy of calcium 59
3.3.1 Ca speciation in thermally treated pine at low oxygen partial pressures 59
3.3.2 Ca nano-mapping by STXM 62

4 Conclusions 64

5 Future research 66
5.1 Ash element characterization 66
5.2 Synchrotron studies 67

Acknowledgements 69

References 71

List of Publications

This thesis is based on the work contained in the following papers, referred to by Roman numerals in the text:

I Thyrel, M., Samuelsson, R., Finell, M., Lestander, T.A. (2013). Critical ash elements in biorefinery feedstock determined by X-ray spectroscopy *Applied Energy* 102: 1288–1294.

II Lestander, T. A., Geladi, P., Larsson, S.H., Thyrel, M. (2012). Near infrared image analysis for online identification and separation of wood chips with elevated levels of extractives *Journal of Near Infrared Spectroscopy* 20 (5): 591–599.

III Thyrel, M., Aulin, R., Lestander, T.A. (2014). Ash content determination of CHP feedstock by ED-XRF and NIR. Submitted manuscript.

IV Thyrel, M., Backman, R., Skyllberg, U., Lestander, T.A. (2014). K-edge XANES characterization of Ca components in thermotreated lignocellulosic biomass destined for pyrolysis or gasification. Manuscript.

V Thyrel, M., Backman, R., Thånell, K., Karunakaran, C., Skyllberg, U., Lestander, T.A. (2014). Nanomapping and speciation of C and Ca in thermotreated lignocellulosic cell walls using scanning transmission X-ray microscopy and K-edge XANES. Submitted manuscript.

The contribution of Mikael Thyrel to the papers included in this thesis was as follows:

I Thyrel planned most of the work, performed laboratory work, XRF measurements and contributed to multivariate statistical modelling. Thyrel wrote the main part of the manuscript.

II Thyrel assisted in planning the work, contributed to the acquisition of NIR images, image analysis evaluation and writing of the manuscript.

III Thyrel contributed in planning the work and performing the laboratory work (XRF pellets and ash contaminations), XRF and NIR measurements and multivariate statistical modelling. Thyrel wrote the main part of the manuscript.

IV Thyrel contributed in planning the work, performed the thermal treatments, contributed to the XANES measurements and performed the XANES data analysis. Thyrel wrote the main part of the manuscript.

V Thyrel planned the majority of the work, performed the sectioning, thermal treatment and FT-IR analysis and also XANES and STXM-NEXAFS data collection and analysis. Thyrel wrote the main part of the manuscript.

Abbreviations

1D-NIR	1-dimensional near infrared
2D-NIR	2-dimensional near infrared
CHP	combined heat and power
ED-XRF	energy dispersive X-ray fluorescence
EXAFS	extended X-ray absorption fine structure
FT-IR	fourier transformed infrared
ICP-MS	inductively coupled plasma mass spectrometry
iPLS	interval partial least square regression
LCF	linear combination fitting
MIA	multivariate image analysis
NEXAFS	near edge X-ray absorption fine structure
NIPALS	nonlinear iterative partial least squares
OD	optical density
OPLS	orthogonal projections to latent structures
PC	principal component
PCA	principal component analysis
PLS	partial least square regression
PLS-DA	partial least squares discriminant analysis
RCG	reed canary grass
RMSEE	root mean square error of estimate
RMSEP	root mean square error of prediction
ROI	region of interest
RPD	ratio of performance to deviation
SIMCA	soft independent modelling of class analogy
SNV	standard normal variate
STXM	scanning transition X-ray microscopy
SVD	singular value decomposition
VIP	variable importance on projection
XANES	X-ray absorption near edge structure
XAS	X-ray absorption spectroscopy
XRD	X-ray diffraction
XRF	X-ray fluorescence

N.B. Matrix notation is used in this thesis: an italic letter indicates a scalar (e.g., K, k), a bold lowercase letter a vector (e.g., $\mathbf{y}$) and bold capital a matrix (e.g., $\mathbf{X}$).

1 Introduction

World energy consumption has more than doubled between the years 1973 and 2011 (IEA, 2013), while at the same time, the world population size has increased from 4 to 7 billion (UN, 2014). Population estimates, though difficult and uncertain, for the year 2050 suggest close to 10 billion people for a medium case scenario, with the main increase predicted to take place in developing countries (UN, 2012). The world energy consumption is expected to increase with population growth and this continuation of unsustainable general consumption and energy usage may have severe environmental, financial and political consequences (Asif & Muneer, 2007; Brennan & Owende, 2010). Specific concerns are the release of greenhouse gases and changes in carbon sink dynamics with imminent global warming (Cox *et al.*, 2000; Zhao & Running, 2010; IPCC, 2013), world oil shortages with large economic effects (Hirsch, 2008; Fantazzini *et al.*, 2011) and political stability issues because only a few countries control a large proportion of the world's oil reserves (Umbach, 2010).

A milestone was passed on May 9, 2013, at the Mauna Loa observatory in Hawaii, when atmospheric CO_2 concentrations reached over 400 ppm for the first time since measurements began in 1958 (NOAA, 2013). Hence, greenhouse gas mitigation seems increasingly important. Non-food biomass as a resource for energy, chemicals and products is considered carbon neutral (Ragauskas *et al.*, 2006), although the issue has been suggested to be more complicated, especially when combustion is taken into account (Johnson, 2009). However, compared to traditional refining using fossil oil and coal, the concept of biorefineries has been proposed as an more environmentally friendly alternative route for producing fuels, chemical and products (Kamm & Kamm, 2004; Corma *et al.*, 2007; Cherubini, 2010). Several types of methodological pathways have been suggested as applicable for biorefinery processes for extracting sugars (mainly from cellulose and hemicellulose) and valuable chemicals, i.e., thermochemical (Haro *et al.*, 2013), chemical (Corma

et al., 2007) and biological (Sanchez & Cardona, 2008). A complicating factor in the biorefinery concept is that biomass as a resource shows large structural and chemical heterogeneity. This heterogeneity necessitates rapid and accurate characterization of feedstocks destined for the different biorefinery processes. The research described in this thesis involved studies on the suitability of using near-infrared (NIR) and X-ray based spectroscopic techniques to study the carbon matrix of selected biomaterials, as well as inorganic components, e.g., ash elements in raw and thermally treated biomass.

1.1 Composition of lignocellulosic biomass

The major structural elements of biomass are cellulose, hemicellulose and lignin, plus additional non-structural elements, such as extractives and inorganic ash elements. Biomass can be divided into broad categories with regard to biological type, source and origin, i.e., woody plants, herbaceous and agricultural plants/grasses, aquatic plants and various waste materials originating from industrial processes. This diversity of biomass sources implies that biomass as a resource for energy and fuels, exhibits large structural and chemical variations. For example, woody biomass can exhibit large variations in cellulose, hemicellulose and lignin, as reported by Vassilev *et al.* (2012), who showed ranges of cellulose of 12.4–65.5 % (mean 39.5 %), hemicellulose of 6.7–65.6 % (mean 34.5 %) and lignin of 10.2–44.5 % (mean 26.0 %). This large variation, which, e.g., depends on species, growth location and soil conditions, makes pre-refining characterization particularly important in biorefinery processes. Moreover, most forms of lignocellulose sources show recalcitrance to the necessary compositional breakdown of the complex organic matrix prior to biochemical refining. This recalcitrance has been identified as one of the biggest obstacles against efficient conversion into precursor components such as sugars (Himmel *et al.*, 2007). For example, lignin strongly inhibits the compositional breakdown of cell wall polysaccharides into sugars (saccharification), which is a common process route for ethanol production (Weng *et al.*, 2008).

In the work described in this thesis, two types of biomass assortments were studied: woody plants (including residues from harvest/processing) and herbaceous plants. The main difference in the compositional polysaccharide matrix between woody and herbaceous plants is that woody plants have slightly lower mean cellulose content (39.5 vs. 46.1 %) but also slightly higher hemicellulose (34.5 vs. 30.2 %) and lignin (26.0 vs. 23.7 %) content (Vassilev et al., 2012 and references therein). Moreover, the levels of extractives are

usually significantly higher in herbaceous plants than in woody plants, i.e., 13.7 vs. 3.1 % (Vassilev *et al.*, 2012). Extractives are a collective term for compounds that can be extracted from biomass using polar and non-polar solvents. Examples of extractive compounds are resins, fatty acids, polyphenols, alkenes, terpenes and terpenoids. Extractives are often formed as a chemical defence mechanism when pests and pathogens attack plants. Extractives have been identified as valuable precursor compounds in biorefinery upgrading processes for producing high value chemicals (Lestander & Samuelsson, 2010). Extractives are not evenly distributed throughout plants and trees. For instance, the sap and heartwood of pine contain different amount of extractives. This complicates the extraction of these fractions since size reduction into chips and powder is often the first pre-processing step. Therefore, techniques need to be developed to effectively utilize the enriched parts of the plants with regard to extractive content, characterization and sorting.

1.1.1 Ash elements

Ash content is an important parameter when considering biomass assortments for potential use via thermochemical conversions for energy and fuels. Tao *et al.* (2012) showed in a review of a large literature dataset on biomass properties that element composition played the largest role in differentiating biomass fuel energy content. The typical ash content of the studied biomass assortments (144 species studied in 260 peer-reviewed articles) in the review was in the range 0.1–26.2 %, with a mean value of approximately 3.5 %. The studied species were all of natural origin and no industrial waste assortments were considered in the study. The latter assortments have been shown to have higher ash contents than those from natural sources; Werther *et al.* (2000) reported ash contents in contaminated industrial waste fractions as high as 41.5 % in sewage sludge. Further, woody biomass has a substantially lower ash content than herbaceous biomass; in the review by Tao *et al.* (2012), the ash content was measured as 0.1–6.4 % (mean 1.9 %) and 1.0–26.2 % (mean 7.0 %) for woody and herbaceous biomass, respectively.

Ash in biomass can be divided into separate groups according to origin and location in the plant, i.e., (i) soil and sand contamination during harvest, storage and handling, (ii) inherent vascular ash, and (iii) structural ash (Kenney *et al.*, 2012). The vascular and structural ash is found within the cells and cell walls, respectively. These types of ash are feedstock specific and are governed by the physiology of the plants, soil conditions, etc. Moreover, ash content

varies among different parts of the plant/tree. For instance, Werkelin *et al.* (2005) found that different parts of spruce (*Picea abies* L.) contained different amounts of ash elements, where the total ash content lay in the order needles>bark>twigs>branches>stem wood.

According to a comprehensive review by Vassilev *et al.* (2010), the most abundant ash elements in plant biomass in decreasing order are Ca, K, Si, Mg, Al, S, Fe, P, Cl, Na, Mn and Ti. The composition of ash elements of woody biomass is often enriched in Ca, Mg and Mn, whereas herbaceous biomass is often enriched in K, P, S and Cl. Typical associations of Ca-Mg-Mn in woody biomass can be carbonates, oxides, hydroxides and oxalates. The corresponding plausible phases for the K-P-S-Cl enrichment of herbaceous biomass are phosphates, sulphates, silicates and some carbonates (Vassilev *et al.*, 2013a).

The amount of contaminated ash is largely determined by the type of harvest, handling and storage techniques used. For instance, the harvest of agricultural crops often introduces exogenous contaminations, e.g., soil and sand, which can have large consequences in subsequent refining steps. The ash content of agricultural biomass of soil origin may also be increased by rain or wind (if conditions are dry, resulting in dust). Contaminated ash originating from soil and sand is often enriched in elements such as Si, Al, Ti and Fe (Jenkins *et al.*, 1998).

1.2 Thermal treatment of biomass at low oxygen partial pressures

De-oxygenation of biomass is a vital route in the biorefinery process chain. Thermal treatment has been proposed as a good candidate among the plethora of possible pre-treatment steps used for the initial decomposition of the recalcitrant cell walls of especially lignocellulosic biomass. Several techniques have been suggested to be appropriate for the thermal pre-processing of biomass prior to biorefining. Examples include torrefaction, which is used to deoxygenate and partially degrade the polysaccharide cell wall matrix in order to facilitate subsequent refining, pyrolysis, which is used for the production of bio-oils destined for direct use or as precursor, and gasification, which is used for the production of precursor molecules.

Torrefaction is a low temperature thermal method for de-oxygenating biomass by thermal treatment at temperatures between 225–300 °C in the absence of oxygen (Prins *et al.*, 2006). The main application of torrefaction of biomass material is for preprocessing purposes and to improve the quality of

the feedstock. For example, torrefaction generates a feedstock with higher energy density (low O/C ratio) compared to raw biomass (van der Stelt *et al.*, 2011). Moreover, reducing the size of torrefied material, e.g., by grinding, has been shown to be more energy efficient (lower energy consumption by 6–10 times) compared to using raw biomass (Phanphanich & Mani, 2011). Furthermore, size reduction of torrefied material generates smaller particles, which are also beneficial for other processes, e.g., gasification (Hernandez *et al.*, 2010).

Pyrolysis is a thermal treatment method for producing solid (char), liquid (bio-oils) and gas fractions in the absence of oxygen. There are several types of pyrolysis processes that can be used depending on the desired end product. For example, conventional pyrolysis utilizes typical temperatures of ~600 °C, a slow heating rate and residence times between 5–30 minutes to produce char, bio-oil and gas (Mohan *et al.*, 2006). Fast pyrolysis is employed at approximately the same temperatures as conventional pyrolysis, but the residence time is of the order of one second in order to minimize secondary reactions and maximize bio-oil conversion (Bridgwater *et al.*, 1999). Several alternative types of pyrolysis have been presented and much research is being conducted (for an excellent review, see Mohan *et al.* (2006) and references therein).

Gasification is a thermal method for producing synthetic gas (syngas), comprising CO, H_2, CO_2 and CH_4, by partial oxidation at elevated temperatures (Hernandez *et al.*, 2010). Typical gasification temperatures are in the range 600–1000 °C, depending on the type of gasification technology used (Kumar *et al.*, 2009). Existing gasification technologies can be roughly divided into three groups: (i) fixed bed, (ii) moving bed, and (iii) fluidized bed gasification, where the latter is the most commonly used today. The three different types produce syngas of various qualities. For instance, syngas produced from fixed bed gasifiers often contains substantial amounts of tar or char due to low heat and mass transfer between the feedstock and gasifying agent (Wang *et al.*, 2008). The produced syngas can either be used directly in gas engines or refined into more valuable fuels and chemicals through different process routes, such as the Fischer Tropsch synthesis of diesel fuel (Tijmensen *et al.*, 2002) and dimethyl ether synthesis (Ng *et al.*, 1999). When conducting thermal processing of biomass, especially pyrolysis at high temperatures and gasification, a critical aspect of the feedstock is the ash element composition. Ash-related complications, such as slagging, sintering, fouling and corrosion, can significantly disrupt the process and lead to substantially increased costs due to operational shutdowns and expensive repairs to equipment. The chemistry behind the abovementioned thermal processing complications is

diverse, and therefore it is crucial to understand how these processes are related to ash element composition in biomass. Slagging, which is the process where bottom ash melts and subsequently solidifies and hardens when the temperature decreases, mostly affects pellet and grate-fired systems. Typical reactions leading to bottom ash slagging often involve K-silicates, K-phosphates and K-Ca silicates (Lindstrom *et al.*, 2007; Xiong *et al.*, 2008; Vassilev *et al.*, 2013b)

Sintering or bed-sintering occurs in fluidized bed systems where sand particles of the bed interact with fuel components to form agglomerates, and if severe, defluidization can occur. Several types of mechanisms for bed sintering have been proposed. For instance, Ohman *et al.* (2000) proposed that bed sintering is initiated by the formation of a sticky coating, consisting of alkali-silicates with alkali probably originating from gaseous forms, homogeneously covering bed particles. Partial melting of the particles occurs and agglomeration increases as the bed particle temperature is increased, and if the process is severe enough, defluidization occurs.

Fouling and corrosion can occur in heat exchangers, super-heaters and convection parts of the thermochemical conversion system. Fouling is the process where gaseous products and fly ash particles adhere to surfaces and filters, reducing heat transfer and compromising the function of filters. Both fouling and corrosion have been shown to be greatly influenced by the condensation of gaseous alkali-chlorides. In order to mitigate high levels of gaseous KCl, it has been shown that by injecting ammonium sulphate, a significant reduction of KCl levels by sulphation can be obtained (Brostrom *et al.*, 2007; Davidsson *et al.*, 2008; Kassman *et al.*, 2013).

Calcium is the most common ash element in woody biomass (Vassilev *et al.*, 2010), whereas calcium oxalate has been reported as a prevalent form of Ca in plants (Schneider, 1901; Gilliham *et al.*, 2011) as well as in woody biomass (Shoulaifar *et al.*, 2013). Calcium in combustion devices is considered non-volatile and most often ends up in bottom ashes. If silica is present as contamination from soil and clay or in fluidized beds as sand, calcium is usually found in various silicates. Despite the non-volatile behaviour of Ca, a considerable proportion of Ca is nevertheless transported upwards in the boiler, ending up as fly ash or deposits on heat transfer surfaces. Small bottom ash particles, as well as micron or submicron particles of Ca, have been suggested to be responsible for the transport of calcium in the flue gas stream. For example, Wu *et al.* (2011) showed that Ca can form submicron particles during the combustion of coal and waste derived fuel and particles with sizes less than 0.2 µm had the highest Ca content.

Calcium may also play a role, along with other nuclei, as seed particles during the first stages of aerosol particle formation.

1.3 Electromagnetic radiation

Electromagnetic radiation is produced by acceleration and deceleration of charged particles, e.g., electrons, which are easy to accelerate due to their small mass, and therefore widely used in practical applications, such as modern X-ray tubes. The electromagnetic spectrum spans from highly energetic and short wavelength gamma and X-rays to low energy radiowaves with wavelengths of several kilometers. The relationship between energy (E) and wavelength (λ) of the energy bearing quanta of electromagnetic radiation, named photons, was discovered by Einstein and can be described by

$$E = \hbar c/\lambda \qquad \text{(eq. 1)}$$

where $\hbar$ is Planck's constant and c is the speed of light. Depending on the region of the electromagnetic spectrum studied, the radiation is commonly expressed in wavelength, frequency or energy.

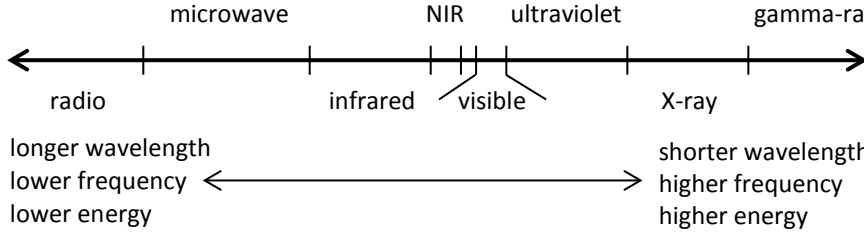

Figure 1. The electromagnetic spectrum ranging from radio to gamma rays.

For instance, when working with the highly energetic radiation of gamma and X-rays, energy is mostly used, expressed in electron volts (eV). On the other hand, when the UV, VIS and NIR regions are studied, the preferred unit is wavelength, often expressed in Ångströms (Å) or nanometers (nm), which correspond to 10^{-10} m and 10^{-9} m, respectively. For the IR region, the number of waves per cm (cm^{-1}) is often used.

1.4 Near infrared spectroscopy (NIR)

Near infrared (NIR) spectroscopy uses electromagnetic radiation in the 780–2500 nm range (Sheppard *et al.*, 1985) and was discovered by Fredrik William Herschel in 1800 (Davies, 1998). Electromagnetic radiation in the NIR region interacts with matter primarily through overtone vibrations originating from fundamental molecular vibrations in the infrared (IR) wavelength range. A molecule can absorb energy if the frequency of the radiation is in resonance with specific molecular vibrations, giving rise to a change in the vibrational energy of a specific bond and subsequent change in dipole moment. In polyatomic molecules, normal modes of vibration, often called fundamental vibrations, involve stretching and bending. The number of ways a molecule can stretch or bend is dependent on the number and configuration of the atoms in the molecule.

Fundamental vibrations can be observed in the mid-IR spectral range, which corresponds to 4000–200 cm^{-1} (2500–50000 nm). In the NIR region, absorption bands mainly correspond to overtones and overtone combinations of fundamental vibrations (Blanco & Villarroya, 2002). The absorption bands in the NIR region are generally broader, overlapping and less intense, often differing by an order of magnitude or more, compared to bands in the mid-IR region. Thus, data interpretation is usually difficult and multivariate statistical procedures are often needed to evaluate NIR data.

NIR has a high penetration depth, and therefore is especially suited for measuring thick samples. NIR techniques have been widely used in both industrial applications as well as academic research. Early applications were targeted toward the agricultural food industry (Kaffka *et al.*, 1982) and were later followed by applications in the pharmaceutical (Reich, 2005), clinical and biomedical (Norris, 1992), and biomass industries (Lestander & Rhen, 2005; Lestander *et al.*, 2009).

1.5 X-ray fluorescence (XRF) spectroscopy

1.5.1 Theory

Electromagnetic radiation in the X-ray region, corresponding to wavelengths of 0.01–10 nm and energies from 150 eV to 100 keV, is used for X-ray fluorescence (XRF) spectroscopy. The X-rays for XRF spectroscopy are commonly produced in vacuum X-ray tubes, wherein electrons are accelerated towards a metal target (anode) that decelerates the impinging electrons and

thus produces a continuous distribution of radiation, named “bremsstrahlung” or breaking radiation, as well as two distinct sharp lines which correspond to the specific anode material in the X-ray tube. These latter lines are called characteristic lines and are the product of the photoelectric effect and subsequent electron transfers within the atoms of the anode material, and thus are element specific. It is therefore not possible to quantify a sample for an element that also makes up the anode target in the X-ray tube due to nested effects.

If high energy particles, such as electrons or X-ray photons, collide with an atomically bound electron and the particle energy is higher than the electron binding energy, an electron is ejected, called a photoelectron. The atom is then left in an excited state. The subsequent events form the basis of XRF spectroscopy, i.e., what happens when an electron from a higher energy level orbital relaxes to a lower energy level orbital. The difference in energy between the corresponding orbitals may result in the emission of an X-ray photon from the atom. A convenient feature that simplifies the analysis of the produced fluorescence photons, discovered by Moseley (1913) and named Moseley’s law (eq. 2), is that their energies are characteristic for specific atoms, and electron transfers and tabulated energy or wavelength values are readily available.

$$1/\lambda = K\,[Z-\sigma]^2 \qquad \text{(eq. 2)}$$

where λ is the photon wavelength, K is a spectral series constant, Z is the atomic number and σ is the shielding constant.

When an excited atom, preferably with an inner core-hole valence, returns to its ground state, a cascade takes place, whereby electrons from higher energy orbitals fill vacancies in inner lower energy orbitals through specific electron transitions. The electron transitions are governed by quantum laws and are divided into so-called normal, forbidden and satellite lines. Normal transitions are most common, thus most intensive and influential for the evaluation of XRF spectra. Examples are the transitions named K_α and K_β which occur when there is an inner (K-shell) core hole. Some transitions appear to contravene the selection rules that quantum mechanics predicts. These transitions are called forbidden and occur when the outer orbitals have unclear energy distinctions, e.g., as is common in the transition elements (Jenkins, 1999). A third transition might also occur, which is related to a process called the Auger process. In the Auger process, an electron in an outer orbital is ejected by the fluorescence radiation produced by the initial excitation, leaving the atom with two

vacancies in the outer orbitals (Jenkins, 1999). This process is also called auto-ionization and leaves the atom in a slightly higher energy level, which results in transitions and subsequent fluorescence signals (called satellite lines) with a slightly higher energy compared when the equivalent transition in a single vacancy excited atom. In the work presented in this thesis, a portable energy dispersive XRF (ED-XRF) analyser was used to observe and analyse the two most prominent normal transitions (K_α and K_β). In Figure 2, a spectrum from a sample of pine branches and tops is presented, which shows the K_α lines of some of the most common elements in biomass materials, as well characteristic lines from the X-ray tube resulting in the so-called scattering region.

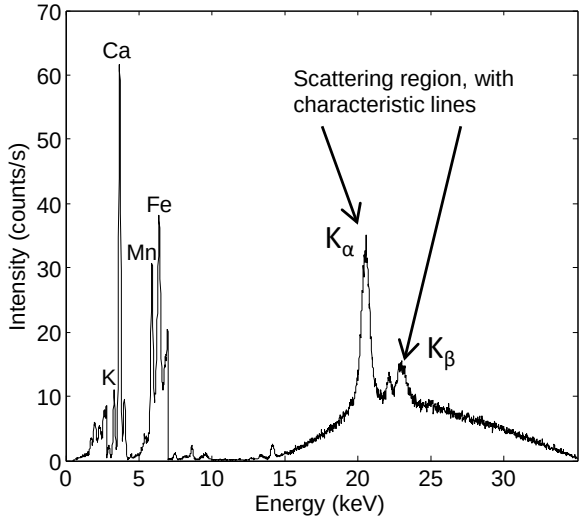

Figure 2. Typical ED-XRF spectrum of a sample of branches and tops collected at a Swedish combined and heat power plant.

1.5.2 Scatter effects

As mentioned above, characteristic lines that originate from the anode materials are produced in an X-ray tube and seen as sharp lines in the otherwise rather smooth distribution of the bremsstrahlung spectra. These lines, which are the product of 2p–1s (K_α) and 3p–1s (K_β) transitions, interact with the sample material through scattering. Scattering can be divided into two types: elastic scattering (also known as Rayleigh scattering), which is a scatter event where no energy loss occurs, and inelastic scattering (also known as Compton scattering), where the particle, often a photon, loses some of its

energy to the electron. These events were evident in all spectra collected and analysed in the present study. This region in the spectra is henceforth referred to as the scattering region.

1.5.3 Fluorescence yield

The fluorescence yield is defined as the probability that an electron valence state will result in a detectable fluorescence photon. The main competing process that negatively influences the probability that an X-ray photon will leave the atom is the Auger process. The fluorescence yield becomes progressively smaller with lower atomic numbers. For example, the fluorescence yield of Na (Z=10) is 2.3 %, whereas the fluorescence yield of Fe (Z=26) is 34.0 % (Krause, 1979). This phenomenon means that the XRF technique is considerably less accurate when measuring light elements (Z<12).

1.5.4 Matrix effects

Analysing XRF data qualitatively is relatively straightforward using Moseley's law or tabulated values. However, when analysing data quantitatively, confounding processes may complicate the analysis, particularly non-linearity interactions may occur between the fluorescence intensity and element concentration. These confounding processes are called matrix effects and are mostly influenced by the presence of other elements embedded in the matrix. There are three main types of matrix effects: (i) differences in the absorption coefficient (μ) of the matrix, which leads to differences in the absorption of the primary radiation, (ii) absorption of the fluorescence radiation from the analyte by the matrix elements, and (iii) the matrix elements may generate fluorescence radiation that is slightly more energetic than the binding energy of core electrons in the analyte, thus enhancing the signal from the primary produced fluorescence photons (Jenkins, 1999).

Sample heterogeneity, albeit not a true matrix effect, can have a large impact on the precision of a measurement and introduce large errors and variances. In fact, improper preparation of samples is often the single largest potential error during an XRF measurement (Beckhoff *et al.*, 2007). Before a sample is measured by XRF, great care should be taken to homogenize the sample to ensure that the top surface of the sample is representative of the whole sample. Grinding the sample in order to achieve uniform particle size is the standard method. However, the grinding equipment needs to be selected carefully because it has been shown that grinding can contaminate the sample (Thompson & Bankston, 1970; Takamasa & Nakai, 2009). Pelletizing the

ground sample is also beneficial because the procedure levels out large density differences and provides a smooth surface in order to minimize unwanted scatter effects of the primary radiation. Grinding and pelletizing were used for all samples analysed by XRF spectroscopy in the present work.

1.5.5 XRF calibration

Calibration with a set of standards usually works well, but if the concentration range is large and matrix compositions differ between samples, problems might arise. During the history of X-ray fluorescence (XRF) spectroscopy, several different kinds of calibration for signal corrections have been developed in order to calibrate the signals from XRF. Addition of internal standards and standard addition have been used for single element quantification and often work satisfactorily. Moreover, the use of background of scattered tube radiation (Compton scattering) as an internal standard has been shown to give quite reliable results for single element quantification (Andermann & Kemp, 1958) and is sometimes included in factory instrument calibrations (Dupyrat. M, Thermo Fisher Sci. Inc, Pers. Comm.).

With the advent of cheap and powerful computers, several multi-element calibrations were developed. One type of matrix correction method utilizes influence coefficients. Influence coefficient methods, developed from the mid-1960s (Lachance & Traill, 1966; Claisse & Quintin, 1967; Rasberry & Heinrich, 1974; Lachance & Claisse, 1980), assume a linear relationship between analyte concentration and its fluorescence signal and any deviations from linearity are attributed to matrix effects (Beckhoff *et al.*, 2007). Based on the work conducted by Sherman (1955), a new type of model was proposed that used fundamental parameter values from Sherman's equations combined with empirical data (Criss & Birks, 1968; Criss *et al.*, 1978). This work was continued by Rousseau, who later proposed the *Fundamental Algorithm* (Rousseau, 1984) for correcting matrix effects, which avoids the use of standards but instead uses theoretical calculations of influence coefficients. Fundamental parameter models are used widely today and yield accurate concentration estimates in XRF analysis. However, for some applications, such as energy dispersive X-ray fluorescence (ED-XRF) where discontinuities in the primary spectrum occurs, the calculations become highly complex and a cheaper easier way, often used by manufacturers, is to use tube scattering methods (Jenkins, 1999).

An alternative way of calibrating XRF spectra is to use multivariate statistical methods such as partial least square (PLS) regression, which has

been shown to function reasonably well (Swerts *et al.*, 1993; Pereira *et al.*, 2006) and is used in the work described in this thesis.

1.6 X-ray absorption spectroscopy

1.6.1 Synchrotron light

X-ray absorption spectroscopy (XAS) has been proposed as one of the most versatile and powerful methods for structural characterization. XAS requires a tuneable X-ray source. Thus, a synchrotron is usually employed to study the absorption of incident X-rays with increasing energy on the sample. Synchrotron light is produced in synchrotron ring facilities, where charged particles, e.g., electrons, are accelerated in a linear accelerator to near the speed of light and then injected in a high vacuum storage ring. Strong magnets control the electrons' trajectory within the ring. The magnetic force on the electrons produce synchrotron light but with relatively low brilliance (photons/s) so insertions devices, which produce alternating magnetic fields by using dipoles of alternating polarity, are injected at straight regions of the ring in order to increase the brilliance of the produced light (photons/s). The insertion devices in third generation storage rings cause the electrons in the ring to undulate from the straight electron path and produce photons at each bend, thereby increasing the flux (Beckhoff *et al.*, 2007).

Furthermore, since the magnetic field can be varied, a substantially larger spectral range can be achieved using insertion devices. The insertion devices used today are either of wiggler or undulator type. Wigglers produce synchrotron light with a broader bandwidth, whereas undulators produce a more brilliant light but with a smaller bandwidth. Both types of device are used in modern synchrotrons and are selected according to the experiment/technique employed. At each insertion device, a so-called end station or beamline is situated, which uses the extracted synchrotron light for specific applications. Most beamlines are equipped with a monochromator. The monochromator typically consists of two parallel crystals that filter away most of the produced bremsstrahlung, producing monochromatic light according to Braggs law (eq. 3).

$$n\lambda = 2d\sin\Theta \qquad \text{(eq. 3)}$$

where n is an integer, λ is the wavelength of the incident wave, d is the spacing of the crystal (atomic lattice) and Θ is the angle between the incident light and scattering planes.

The first crystal monochromates the light, whereas the second crystal is often used for detuning, i.e., filtering away higher order harmonics. After the monochromator, an optic system consisting of mirrors for polarization and slits is often used to regulate the flux of light impacting the sample.

1.6.2 Absorption measurements

XAS is a spectroscopic technique in which the absorption of a known quantity of incident X-ray radiation is measured after the X-rays pass through the sample, as shown in Figure 3.

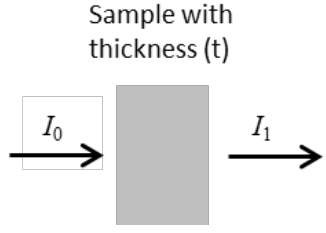

Figure 3. Typical arrangement for an XAS experiment in transmission mode

As suggested by its name, X-ray absorption spectroscopy primarily deals with the absorption characteristics of a material described by its absorption coefficient (μ). The absorption coefficient can be defined using the Lambert-Beer law (eq. 3):

$$I=I_0e^{-\mu t} \qquad \text{(eq. 3)}$$

where I and I_0 are the transmitted and incident X-ray intensity, respectively, μ is the absorption coefficient and t is the sample thickness.

XAS thus involves the study of the absorption coefficient of a sample irradiated with X-rays of increasing energy over the so-called absorption edge. The absorption of X-rays decreases with increasing energy, but a sharp rise in absorption occurs when the incident energy of the absorbed photon equals the binding energy of a core electron and a photoelectron is produced (Figure 4). The absorption edges thus correspond to the different electron binding energies of, e.g., the K and L shells in the absorbing atom, i.e. the 1s and 2p/2s electron orbitals, respectively. These energies have been thoroughly investigated and tabulated, e.g., see Williams (2009).

The threshold energy (E_0) at the absorption edge, which is defined as the energy where a photoelectron is released, is often selected as the first inflection point of the collected absorption spectrum. Absorbed photons on the lower energy side of E_0 potentially give rise to pre-edge features corresponding to electronic transitions to unoccupied or partially filled energy levels of the atom. If the photon energy of the incident radiation (E) is close to E_0, electron transitions occur to either unfilled orbitals or the continuum. Finally, if E is larger than E_0, electron transitions occur to the continuum with a kinetic energy (E_k) of $E_k=E-E_0$.

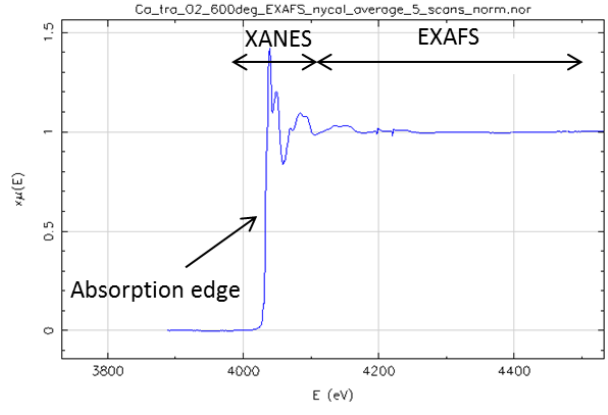

Figure 4. Calcium XAS spectrum of a thermally treated pine sample.

In XAS theory, it is convenient to envision the photoelectron quantum mechanically, depicting its behaviour as a wave, referred to as a photoelectron wave. The photoelectron wave backscatters from surrounding atoms and constructive/destructive interference between the outgoing and backscattered photoelectron waves takes place as E_k is increased during an XAS measurement. The constructive and destructive interference increases and decreases the electron density, respectively, giving rise to oscillations of the absorption and are the basis for XAS measurements.

Absorption spectra have traditionally been divided into two parts: the X-ray absorption of near edge structure (XANES) region, which stretches from -10 eV to +50 eV from the absorption edge, and the extended X-ray absorption of fine structure (EXAFS) region, which begins at + 50 eV and stretches several hundreds of eV from the absorption edge (Figure 4).

One major advantage of using XAS spectroscopy is that crystalline, amorphous solids as well as solutions can be measured. XAS can be performed in transmission mode, whereby the intensity of the radiation is measured by employing an ion chamber filled with an appropriate gas before (I_0) the perpendicularly placed sample and another ion chamber after the sample (I_1). Often a third ion chamber (I_2) is used after an appropriate reference foil in order to put the measurement on an absolute energy scale.

The transmission mode is the preferred method when the absorber concentration is high and specimen thickness is sufficiently thin. If the absorber concentration is low and diluted, or of low atomic number, it is often beneficial to measure in fluorescence mode which is made possible since the production of fluorescence photons is proportional to the absorption. The experimental setup for measurements in fluorescence mode usually involves placing the sample at 45° and the detector orthogonal to the incident beam.

1.6.3 EXAFS

The mathematical description of the EXAFS part of the spectra will only be discussed briefly since it was not used in the work described in this thesis. The system investigated in Paper IV had several phases present in natural samples, and thus produced complex spectra that were difficult to deduce with the EXAFS technique. Therefore, EXAFS works better with simpler systems, e.g., single and binary systems are much more informative because they yield sharp distinct peaks in the derived EXAFS spectra (Persson, I. 2014, pers. comm.). Furthermore, the collected EXAFS spectra at the K-edge of calcium were of poor quality and the oscillations decayed after $k>6$.

The steps involved in EXAFS analysis after acquiring the spectra are summarized below (Newville, 2004):

- Convert measured intensities to $\mu(E)$.
- Perform energy calibration using a signal from metal foil, collected after the sample, or use a standard measured between sample acquisitions.
- Fit a pre-edge spline in order to remove instrument noise, etc.
- Determine E_0.
- Fit a post-edge spline in order to isolate the small oscillations corresponding to the EXAFS signal.
- Normalize $\mu(E)$ to vary from 0 to 1 so that it represents the atomic background of a single atom of the absorbing element.

- Calculate the experimental EXAFS signal from $\chi(E)=[\mu(E)-\mu_0(E)]/\mu_0(E)$.
- Convert the EXAFS signal (from eV to wavenumbers) into k-space by using $k=(2m(E-E_0)/\hbar^2)^{1/2}$ ($Å^{-1}$).
- k-weight the EXAFS.
- Perform Fourier transformation for conversion into R-space (Å) in order to study bond distances, angles, etc.
- For validation, calculate the theoretical EXAFS signal for plausible structures using Feff codes (Rehr *et al.*, 1991).

1.6.4 XANES

It has been proposed that the XANES part of the spectrum should be divided into XANES and near edge X-ray absorption of fine structure (NEXAFS) regions (Rehr *et al.*, 1998) due to better understanding of the complex photoelectron wave behaviour in the edge region, i.e., improved multi-way scattering theory. In this thesis, the older classification is used for XANES, stretching from -10 to +50 eV. Additionally, since XANES has significantly larger signals compared to the small oscillatory signals of EXAFS, it can be applied for lower sample concentrations and sub optimal sample conditions. The term NEXAFS is also often used to refer to the soft X-ray region but the signals cannot usually be modelled by scattering theory and such models. Thus, in practice, it is an XANES spectrum at lower energies.

Even though XANES cannot be fully interpreted theoretically because the EXAFS equation breaks down at low *k*-values due to multiple scattering, etc., the region still contains a lot of useful chemical information. The XANES region shows distinct features that relate to the specific photoelectron transitions within the absorbing atom. These spectral features provide information on various structural parameters:

- Oxidation state.
- Coordination chemistry – regular/distortions in structure as well as structural components (tetrahedral, octahedral, etc.).
- Molecular orbitals – orbital hybridization (*p* or *d*).

One of the most common applications of XANES utilizes the shift of the absorption edge (E_0) position to determine the oxidation/valence state and coordination environment (Newville, 2004). For instance, one unit of oxidation state change can shift the edge position by several eV due to changes in the energy of the photoelectron transition within the absorber (Coppens *et al.*,

1992). Moreover, when studying transition metal oxides, where *p* or *d* orbital hybridization is substantially altered depending on the coordination environment and valence state as the number of available *d* electrons vary, clear differences in the absorption spectra are found (Newville, 2004). The pre-edge region of XANES often has small peaks attributed to 1s–3d transitions (Grunes, 1983), which are also useful for structural determination. Thus, in summary, XANES can be used as a fingerprinting tool for quantitative, or at least semi-quantitative, analysis of unknown spectra, providing that suitable model compounds are available for comparison.

The initial steps in analysing XANES are the same as for EXAFS analysis, i.e., convert to $\mu(E)$, energy calibration, pre- and post-edge spline fitting, and finally, normalization of the signal to a value between 0–1, representing the absorption of a lone atom. Since the EXAFS equation is not applicable, one commonly used technique for assessing the valence state and phases present in a sample is linear combination fitting (LCF). In LCF, a set of measured spectra from reference compounds is used to obtain an optimal fit to an unknown sample spectrum by non-linear least square minimization. This is an iterative method and the algorithm attempts to minimize the residual between combinations of reference spectra to the model unknown spectrum. Other data analysis techniques, such as principle component analysis (PCA) and factor analysis, are also commonly used for XANES interpretation.

As a final note, self-absorption is a recurring problem that has to be taken into consideration, especially when performing XAS spectroscopy in fluorescence mode. Self-absorption is the process where the sample itself absorbs produced fluorescence photons, yielding smeared spectra with diminished spectral features. This can be avoided by using diluted thick samples or very thin concentrated ones, depending on sample type.

1.7 X-ray diffraction (XRD)

The X-ray diffraction (XRD) technique is a powerful technique for analysing crystalline phases in solids. The technique studies the diffraction of almost monochromatic X-rays by a crystal lattice according to Bragg's law (Jenkins, 1999):

$$\lambda = (2d/n)\sin\Theta \qquad \text{(eq. 4)}$$

where λ is the wavelength of incident radiation, d is the planar spacing in the crystal lattice, n is an integer and Θ is the angle between the scattering planes and incident radiation.

The angle at which diffraction occurs is measured with high accuracy due to the instrument setup (detector and X-ray tube mounted on a goniometer), and a diffraction pattern is collected as the Θ angle is increased. Comparison with diffraction spectra from known structures (crystallographic databases) enables identification of phases in a sample.

1.8 Scanning transmission X-ray microscopy (STXM)

The need for nanostructured probes led to the development of the scanning transmission X-ray microscope (STXM), which was first constructed at National Synchrotron Light Source at Brookhaven National Laboratory, USA. This technique, depicted in Figure 5, requires monochromatic X-rays that can be provided from a synchrotron source and is an imaging technique capable of a spatial resolution of the order of tens of nanometers, where a NEXAFS spectrum is recorded for each pixel.

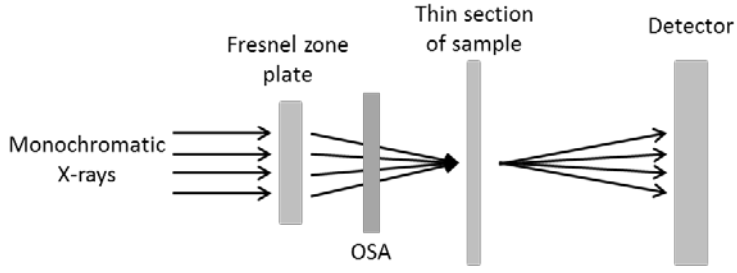

Figure 5. Schematic showing a scanning transition X-ray microscope (for description, see text).

X-rays are focused on the sample using a Fresnel zone plate, which is capable of focusing the X-rays to a spot size of the order of tens of nanometers (currently 20–30 nm at best). An order sorting aperture (OSA) is placed before the sample in order to filter higher order harmonics of the diffracted light. The X-rays are transmitted through the sample and the detector measures the transmitted intensity. The intensity can be converted to optical density (*OD*) according to eq. 5:

$$OD = \ln(I_0/I) \qquad \text{(eq. 5)}$$

where ln is the natural logarithm, I is the transmitted X-ray intensity through the sample and I_0 is the X-ray intensity recorded along the same optical path but without the sample. The sample is placed on a moving sample stage

controlled by piezoelectric motors, which enable *x*, *y* and *z* movement of the sample, thus allowing X-ray images to be scanned successively pixel by pixel. Typical dwell times for pixel acquisition are 0.5–1 ms. Successive images of the sample over the absorption edge of the element in question are recorded and a collection of images, often referred to as a stack, is acquired.

Reference compounds, obtained with the same energy increments as the sample stack, can be used for thickness evaluation (by using singular value decomposition) if the mass absorption coefficients for the reference compounds are known. Pixel-wise LCF analysis can also be performed for reference compounds, assuming that the overall OD is similar. Furthermore, multivariate analysis techniques, such as PCA, are commonly used to perform cluster analysis of the pixels in the acquired hyperspectral image stack.

1.9 Multivariate statistics

With the introduction of modern spectroscopic techniques, generating huge amounts of data, multivariate statistics is often necessary for extracting the requested information. This is especially the case when the number of samples, referred to as observations, is small compared to the number of variables or data points, which often leads to co-linearity issues, greatly complicating univariate analysis. There are several types of multivariate statistical procedures used in: screening, classification, calibration etc. Prior to performing a multivariate statistical analysis, it is often a good idea to compute basic statistics of the dataset, such as mean values, standard deviation, minimum and maximum values, in order to get a general idea of dataset boundaries and ranges. For instance, severe outliers can greatly influence several multivariate techniques, directing the model in the wrong direction in multivariate space.

1.9.1 Principal component analysis (PCA)

Principal component analysis (PCA) is an unsupervised multivariate technique that is an excellent approach for finding patterns in large datasets, especially for highly collinear data, such as NIR and XAS spectra. PCA is basically a compression technique, whereby multi-dimensional data is projected to a few low dimensional planes by using sets of bi-linear functions, called principal components (PCs), to capture as much of variance as possible. The PCs are placed in order of decreasing amount of variance explained and are positioned orthogonal to the last placed and normalized PC.

PCA was introduced by Pearson (1901) and later refined by several researchers (Jolliffe, 1986; Wold *et al.*, 1987). Several algorithms are used for PCA, the most common are singular value decomposition (SVD) (Golub & Reinsch, 1970) and nonlinear iterative partial least squares (NIPALS) (Wold, 1966). In matrix notation, PCA can be described by

$$\mathbf{X} = \mathbf{T}\mathbf{P}^{\mathrm{T}} + \mathbf{E} \qquad \text{(eq. 6)}$$

where $\mathbf{X}$ is the raw data matrix (often mean-centred) with a size of ($I \times J$), $\mathbf{T}$ ($I \times A$) is a matrix of score vectors with A the number of PCs, $\mathbf{P}$ ($J \times A$) is a matrix of loading vectors and $\mathbf{E}$ ($I \times J$) is the residual matrix.

The score vectors are derived by projecting the sample points (observations) onto the PCs. By studying the score vectors of **T**, relationships between observations can be found. The loading vectors are the weight that each original variable had when the PC was computed. By studying the loading vectors of **P**, connections between variables can be resolved. If scores and loadings are studied in conjunction, the loading can explain the score values of individual observations on specific PCs.

The most common way of evaluating a PCA model is to study the score plot, where the observation scores of individual PCs are plotted. PCA models were constructed for all datasets acquired in the present work, either as a separate analysis or to detect outliers and observations that greatly skew the direction of the first PC, identify groupings and obtain a general overview of the data.

1.9.2 Partial least squares (PLS) regression

Partial least squares (PLS) regression is an iterative method for relating a predictor or variable matrix and a response vector or matrix. It was originally based on the NILIS algorithm developed by Herman Wold (Wold, 1966). The predictor matrix, denoted **X**, is often a matrix derived from more easily acquired data, such as spectroscopic data, whereas the response vector, denoted **y**, is made up of responses, e.g., in chemistry, the latter is often obtained by fairly tedious wet chemical analysis.

There have been several suggested modifications and alternatives to the original PLS algorithm (Martens & Jensen, 1983; Martens & Næs, 1987; Dejong, 1993), later called NIPALS (Wold, 1975). A distinction can be made between the two most commonly used algorithms, NIPALS and the Martens algorithm. Whereas the NIPALS algorithm uses orthogonal PLS factorization,

the factorization of the Martens algorithm produces non-orthogonal PLS score vectors that contain co-linearity. None of these algorithms produce fully orthogonal loadings and orthonormal scores like those in PCA. Ergon (2002) has therefore proposed SVD composition of PLS solutions to obtain orthogonal loading vectors and orthonormal score vectors. Furthermore, this solution of bi-orthogonal PLS regression offers a standardized way of interpreting results independent of the applied PLS algorithm.

PLS is a common method for constructing calibrations. Based on a response vector (**y**), the general equation of PLS is shown in eq. 7.

$$\mathbf{y}=\mathbf{X}\mathbf{b}_{pls}+\mathbf{f} \qquad \text{(eq. 7)}$$

where **y** is a vector of responses, **X** is a matrix of variables for the observations, e.g. spectroscopic data, **b** is a vector of computed PLS coefficients and **f** is the vector of residuals.

One common use of PLS is the construction of multivariate calibration models, which can be used to predict unknown samples. By using part of the sample set (calibration set) for constructing the PLS calibration model, the remaining samples can be used as a test set for evaluating the predictive ability of the model. As general rule of thumb, 2/3 of the samples are usually used for the calibration set and the remaining 1/3 for the test set. If the number of samples is limited, cross validation is a common way of measuring the calibration models ability to predict new samples. Several different regimes are used, such as leave-one-out (L1O) or venetian blinds, where one or more samples are left out of the calibration and predicted by the model, and in the next step, other samples are left out and so forth until all samples have been left out once.

Another important consideration when constructing PLS models is the pseudorank of the model, i.e., the number of PLS components or latent variables, often denoted A, that are used for constructing the model. If A is too small, a considerable amount of the predictive variation may be left un-modelled and the model is said to be under-fitted, resulting in poor prediction capabilities. If A is too large, the model is probably over-fitted with possible noise contributing to the calibration model, yielding a good fit but once again poor predictive capabilities. The appropriate number of PLS components for the constructed calibration models described in Paper I and III were determined from the first minimum in the root mean square error of prediction (RMSEP), unless the minimum was in the first or second component because this might have indicated severe under-fitting of the complex calibration models.

1.9.3 Diagnostics

To test the usefulness and accuracy of constructed calibration models, several diagnostics are commonly employed. The majority of diagnostic tools used in studies described in Paper I–III were based on the vector of residuals from the test set ($\mathbf{f}_t$)**,** thus reflecting the predictive behaviour of the model. The root mean square error of estimate (*RMSEE*) is on the other hand based on the vector of residuals from the calibration set ($\mathbf{f}_c$), thus reflecting the errors associated with the calibration model itself and disregarding the predictive ability of the model.

Listed below are the diagnostics used in Paper I–III. The coefficient of multiple determination (R^2) of the calibration set describes the amount of variation explained by the model:

$$R^2 = 1\text{-}\mathbf{f}_c^T\mathbf{f}_c\,(\mathbf{y}_c^T\mathbf{y}_c)^{-1} \qquad \text{(eq. 8)}$$

where ($\mathbf{y}_c^T\mathbf{y}_c$) is the sum of squares for the mean-centred response ($\mathbf{y}$) in the calibration set and $\mathbf{f}_c^T\mathbf{f}_c$ is the sum of squares for the residual vector from the calibration.

Similarly, the amount of described variation in the test set (Q^2) can be described by eq. 9:

$$Q^2 = 1\text{-}\mathbf{f}_t^T\mathbf{f}_t(\mathbf{y}_t^T\mathbf{y}_t)^{-1} \qquad \text{(eq. 9)}$$

where ($\mathbf{y}_t^T\mathbf{y}_t$) is the sum of squares for the mean-centred response ($\mathbf{y}$) of the observations in the test set and $\mathbf{f}_t^T\mathbf{f}_t$ is the sum of squares for the residual vector from the validation of the test set.

As was mentioned earlier, *RMSEE* is used to describe the mean error in the calibration model, as shown in eq. 10**:**

$$RMSEE = [\mathbf{f}_c^T\mathbf{f}_c(I\text{-}A\text{-}1)^{-1}]^{1/2} \qquad \text{(eq. 10)}$$

where $\mathbf{f}_c^T\mathbf{f}_c$ is the sum of squares of the residual vector of the calibration set, I is the number of observations and A is the number of PLS components.

The mean error in prediction is frequently presented as the root mean square error of prediction (*RMSEP*) and is shown in eq. 11:

$$RMSEP = [\mathbf{f}_t^T \mathbf{f}_t J^{-1}]^{1/2} \quad \text{(eq. 11)}$$

where $\mathbf{f}_t^T \mathbf{f}_t$ is the sum of squares for the residual vector of the test set and J is the number of observations in the test set.

Bias is an important diagnostic tool that can show whether the randomly chosen samples of the test set are representative. Large values of bias indicate systematic errors that need to be addressed. For example, in calibration transfers between instruments, large biases can occur, even though the precision might be good. Measures that can be taken to limit the bias in such circumstances include the introduction of off sets. Large biases indicate non-representative test samples, and consequently a larger *RMSEP*.

$$Bias = \mathbf{1}^T \mathbf{f}_t J^{-1} \quad \text{(eq. 12)}$$

where $\mathbf{f}_t$ is the vector of residuals from the test set and J is the number of observations in the test set.

The ratio of performance to deviation (RPD) is a diagnostic tool proposed by Williams and Sobering (1993) that relates the prediction error (*RMSEP*) to the length of the response vector y (standard deviation). The classification adopted by Saeys *et al.* (2005) is used for assessing the usefulness of the calibration: $RPD < 1.5$ indicates an unusable calibration, $1.5 < RPD < 2$ indicates a model that can distinguish between high and low values, $2 < RPD < 2.5$ indicates a model with approximate quantitative predictability, *RPD* values between 2.5 and 3, and >3, indicate that the predictive accuracy is good and excellent, respectively. The calculation of *RPD* is described in eq. 13:

$$RPD = [\mathbf{y}_t^T \mathbf{y}_t (J\text{-}1)^{-1}]^{1/2} [\mathbf{f}_t^T \mathbf{f}_t J^{-1}]^{-1/2} \quad \text{(eq. 13)}$$

where $\mathbf{y}_t^T \mathbf{y}_t$ is the sum of squares for the mean-centred response ($\mathbf{y}$) of the test set, $\mathbf{f}_t^T \mathbf{f}_t$ is the sum of squares for the residual vector of the test set and J is the number of observations in the test set.

When evaluating a PLS model, it is often useful to establish which variables (energies or wavelengths) have the greatest impact on the model. One way of doing this is to study the variable importance on projection (*VIP*), which was developed by Wold (1994) and is shown in eq. 14:

$$VIP_k = \{[\mathbf{w}_k^2 \mathbf{s}^T][(\mathbf{y}_{p,A}^T \mathbf{y}_{p,A} (\mathbf{y}^T \mathbf{y})^{-1}) K^{-1}]^{-1}\}^{0.5} \quad \text{(eq. 14)}$$

where k is the individual variable (energy or wavelength), **w** and **s** are weights and scores, respectively, $\mathbf{y}_{p,A}{}^{T}\mathbf{y}_{p,A}$ is the sum of squares for the mean-centred response for the chosen PLS component, ($\mathbf{y}^{T}\mathbf{y}$) is the total sum of squares of the response and K is the total number of variables (energies or wavelengths).

In Paper I, additional diagnostics were calculated to evaluate the precision of measurements, detection limits and relative prediction error.

1.9.4 Multivariate image analysis (MIA)

Several spectroscopic techniques offer possibilities for combining imaging with obtaining spectral and spatial information on various scales, where the spatial resolution often is determined by the wavelength of the radiation. Examples of modern spectroscopic imaging techniques are NIR, FT-IR, Raman and X-ray techniques, such as STXM. A common feature of these techniques is that they produce hyperspectral images, i.e., layered images that can consist of several hundreds of individual layers. An example of a hyperspectral image is shown in Figure 6.

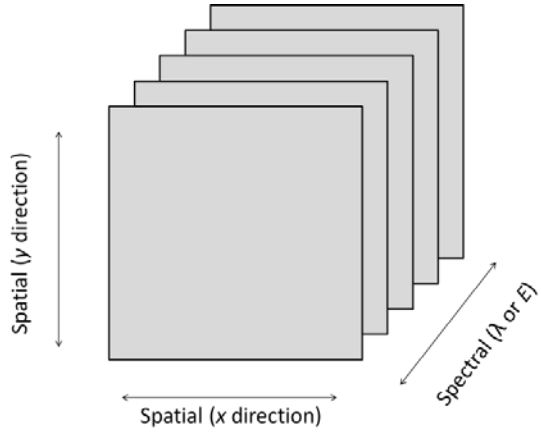

Figure 6. Schematic of a hyperspectral image in spatial x and y directions at different wavelengths (λ) or energies (E).

Hyperspectral images often contain large amounts of data. For instance, a typical STXM image with dimensions 120 by 120 pixels and 94 energies (120×120×94) equates to 1.35 million data points. This suggests that it is most practical to analyse these kinds of data by using multivariate techniques, for example PCA or PLS. The early work of Geladi *et al.* (1986) lay the foundations for multivariate image analysis (MIA).

One cannot perform ordinary PCA directly on a three-dimensional data structure, but instead, the matrix needs to be unfolded. Unfolding is performed pixel-wise over the length of the spectra, resulting in a two-dimensional matrix where each row represents a pixel spectrum. Thus, the dimensions of the abovementioned unfolded STXM image would be 14400×94. Information on the spatial location of each pixel is saved to facilitate back-folding of the two-dimensional matrix into a three-dimensional data structure after the multivariate analysis has been performed.

PCA is an excellent technique for data compression. The projection to fewer dimensional planes obtained from pixel score values presented in score plots can be very informative, both for detecting patterns or groups in the data as well as identifying outliers. The detection and handling of outliers, i.e., strongly deviating observations that have a large influence on the multivariate models, are particularly important (Martens & Næs, 1989; Daszykowski *et al.*, 2007).

Spectral preprocessing is often performed before analysing hyperspectral images because the vast set of spectra acquired is likely to contain individual or groups of pixel spectra that are dissimilar from the rest. These spectra are often considered erroneous or noisy and may derive from instrument errors (source and detector inconsistencies), sample differences (particle size, density) and scatter effects. Several techniques are commonly employed for adjusting the scale and limiting model contributions from noisy and baseline variations. Examples of such techniques include the use of derivative and smoothed spectra, e.g., Savitzky-Golay functions (Savitzky & Golay, 1964); multiplicative scatter correction (MSC) (Geladi *et al.*, 1985), which aims at reducing scaling and baseline effects based on scatter; standard normal variate (SNV) transformation, which aims at reducing multiplicative scatter effects (Barnes *et al.*, 1989); and orthogonal scatter correction (OSC) (Wold *et al.*, 1998), which removes noise that is uncorrelated to the response data, e.g. **y** vector.

Moreover, Trygg and Wold (2002) have proposed an alternative preprocessing method of removing variation in **X** that is uncorrelated to **y** data. They named the algorithm orthogonal projections to latent structures (OPLS). In OPLS, non-correlated variation in **X** is removed for each PLS component. This makes the PLS model interpretation easier and allows the uncorrelated variation to be analysed as well.

A particularly useful technique when analysing hyperspectral images, explored by Esbensen and Geladi (1989), is the brushing technique, which nowadays is incorporated in some MIA software, e.g., Evince (Umbio AB, Umeå Sweden). The brushing technique is based upon correlation between, for

instance, a PCA score-plot and the corresponding raw image. Pixels in the raw image are selected and the corresponding pixels in the score-plot are highlighted and vice versa. This feature enables easy identification of outliers caused by, e.g., edge effects and their subsequent removal. Moreover, groups of pixels with similar scores are easily identified in the score plot and spatial information can be extracted.

PCA is probably the most commonly used MIA technique, but a number of other techniques have also been extensively used. PLS-based discriminant analysis (PLS-DA) is a supervised technique where a number of categorical response variables are introduced, referred to as dummy variables, which describe class membership of the observations in the training set. A PLS is performed relating **X** and the introduced dummy variables and validated by using a test set. PLS-DA has been shown to function well with 2–4 classes. (Eriksson *et al.*, 1999). Another widely used technique is soft independent modelling of class analogy (SIMCA) modelling (Wold *et al.*, 1984). In SIMCA modelling, an initial PCA of the whole dataset is conducted and groups of observations are selected into classes. Local PCA models are then calculated for each class and cross-validation is performed in order to estimate the number of components for each class. New observations can then be classified by calculating the residual variance based on the fit for each respective local model. If the residual variance is too large the sample will be unclassified and either treated as an outlier or part of a class that is unknown to the model.

1.10 Objectives

The overall objectives for the research that formed the foundation of this thesis were to study the applicability of different X-ray and infrared spectroscopy techniques for characterizing and classifying potential lignocellulosic biomass materials destined for biorefinery purposes.

Specific objectives were to

- Study the suitability of using PCA and XRF spectroscopy for separating different types of solid biofuels (Paper I).
- Construct robust PLS calibration models for ash related elements and total ash content for different kinds of biomass samples (Paper I).
- Use 2D-NIR spectroscopy for simulated on-line measuring of wood chip extractives to assess the possibility of detecting individual wood chips with high extractive content (Paper II).

- Compare the prediction performance of XRF and NIR spectroscopy on the ash content of biomass samples from CHP production with or without obvious exogenous contaminations (Paper III).
- Study calcium speciation in thermally treated pine powders at low oxygen partial pressures using XANES spectroscopy (Paper IV).
- Perform carbon and calcium nanoscale characterization of thermally treated RCG using synchrotron-based STXM-NEXAFS spectroscopy (Paper V).

2 Material and methods

A summary of biomass materials, analytical methods and instruments, multivariate statistics and software used in the research for Paper I–V is presented in Table 1 and 2.

Table 1. Overview of materials, analytical methods and instrumentation used for the work described in Paper I–V. Paper I–III focus on XRF and NIR studies of biomaterials and Paper IV–V focus on X-ray absorption measurements.

Studies based on:	Paper				
	I	II	III	IV	V
Materials					
Various biomass powders	x		x		
Chips, pine and spruce		x			
Powder, pine				x	
Powder, RCG, variety Palaton					x
Ultra-sections, RCG, variety Palaton					x
Analytical methods and instruments					
- XRF	x		x		
- 1D-NIR		x	x		
- 2D-NIR		x			
- XANES				x	x
- STXM-NEXAFS					x
- FT-IR					x
- XRD				x	x
- Cryo microtome					x
- TGA				x	

Table 2. Overview of multivariate modelling techniques and software used in the studies reported in Paper I–V.

Studies based on:	Paper				
	I	II	III	IV	V
Modelling					
PCA	x	x	x	x	x
PLS	x	x	x		
iPLS	x				
Variable selection	x				
LCF				x	x
Software					
- Matlab	x	x	x	x	x
- PLS Toolbox	x		x		
- SIMCA	x				
- Athena				x	
- Evince		x			x
- Axis2000					x
- Stack-Analyse					x
- FactSage				x	
- ImageJ					x

2.1 Biomaterials and pre-treatments

A wide range of lignocellulosic biomass materials was used for the research presented in this thesis. In Paper I, four species were chosen as biomass models, representing a wide range of compositionally different biomass materials. Gymnosperms were represented by 14 samples of Scots pine (*Pinus sylvestris* L.) sawdust. Angiosperms were represented by 18 samples of hemp stems (*Cannabis sativa* L.), 10 samples of olive fruit kernels (*Olea europea* L.), and 10 samples of grape fruit kernels (*Vitus vinifera* L.). The elemental composition and ash content of these samples had been established beforehand by ICP-MS according to European Standard EN 13656 and EN 14775:2009, respectively. The 119 samples of biomass material collected at 24 Swedish

combined heat and power (CHP) plants, studied in Paper III, were all forest based, ranging from pure stem wood and bark fractions to mixtures of chipped tree tops and branches as well as demolition wood. All biomass materials used for the work described in Paper I and III were oven-dried at 105 °C overnight and milled over a screen with a size of <1 mm. One gram of each sample was compressed into a pellet 13 mm in diameter using a hydraulic press (Specac P/N 15.001, Specac, Graseby, UK) under a pressure of 100 kPa, which was sustained for 30 seconds before removal. The CHP plant samples were analysed for ash content according to EN 14775:2009.

For the work discussed in Paper II, Scots pine and Norway spruce (*Picea abies* (L.) Karst.) were chosen as biomass models for softwood species. Samples were collected from six trees and partitioned into; juvenile sapwood and heartwood; mature sapwood and heartwood; and finally knot wood, resulting in five classes. Partitioning was conducted using a chainsaw and the subsequent chipping was conducted using a chipper (Edsbyhuggen 250 H, Woxnadalens Energi AB, Edsbyn, Sweden). The chips were dried at 60 °C to a 4–5 % moisture content (wet basis).

In the work reported in Paper IV, Scots pine was studied in powder form originating from saw mill waste (Samuelsson *et al.*, 1995) which was milled over a screen size of 1 mm. One gram of powder were thermally treated in oven at temperatures of 300, 350, 400, 450, 500, 550, 600, or 800 °C for 600 s, excluding ramping time, under an atmosphere of pure nitrogen (N_2) or nitrogen containing either 3 vol. % oxygen (O_2) or 6 vol. % O_2. Total gas flow was set to one litre per minute and the oven was overflowed for 30 minutes before starting each experiment. The temperature was continuously monitored. Cooling and post sample treatment were conducted in N_2 atmosphere. The sample transfer to the specialised sample holders for XANES measurements were conducted in a glove box under Argon atmosphere.

Finally, in the work presented in Paper V, reed canary grass (RCG, *Phalaris arundinacea* L.) was studied in powder form (Samuelsson *et al.*, 1995) as well as cross-sections of internode straw for the X-ray imaging. Ultra-sectioning was performed using a cryotome (Leica EMUC7, Leica Microsystems, Wetzlar, Germany) at -18 °C to approximately 100 nm thickness and then transferred to 100 nm thick silicon nitride windows (Si_3N_4, Norcada Inc., Edmonton, Canada) before thermal treatment. Thermal treatments at 300, 400 and 500 °C were performed using the same protocol as was used in Paper IV except that only N_2 atmosphere was used, and the treatment time was limited to 300 s, excluding ramping time.

2.2 Analytical methods and instruments

In order to measure the inorganic composition of the biomass materials studied in the work reported in Paper I, as well as the ash content in Paper III, a portable ED-XRF instrument (Niton XL3t, Thermo Scientific Niton, Billerica, MA, USA) was used. The instrument, which was positioned in a stationary test stand, was equipped with a 50 kV X-ray tube with an Ag target and Si(Pin)-detector. The measurement time was 90 seconds divided into three intervals with corresponding filter settings, to obtain an XRF spectrum from 0–35 keV. Each sample was placed in a measuring cup with a thin mylar film (TF-160-255, Premier Lab Supply, Port St. Lucie, Fl, USA) at the end facing the instrument. For the study described in Paper I, measurements were conducted under a helium atmosphere on pelletized samples at both sides of the pellet and mean spectra from the dual measurements were used. In the work reported in Paper III, a helium atmosphere was not employed. Since the ED-XRF instrument automatically adjusted the X-ray tube flux to minimize overload and dead-time of the detector, normalization of the spectra with regard to the X-ray tube current was performed prior to statistical analysis.

The 1-D NIR spectroscopy employed to model ash content in CHP samples presented in Paper III was performed by using a NIR spectrometer (NIR DA7250, Perten Instruments, Hägersten, Sweden) equipped with an InGaAs detector. Spectra were collected in reflectance (**r**) mode from 950 nm to 1650 nm and log-transformed into absorbance (**a**) according to $\mathbf{a}=-\log(\mathbf{r}^{-1})$. A mirror cup, designed for small samples, were used to collect six average spectra from both sides of the pellet and PCA (Wold *et al.*, 1987) was used for outlier detection. Mean spectra for each sample were calculated. For the 1-D NIR measurements reported in Paper II, a NIR spectrometer (Foss NIRSystems, Höganäs, Sweden) was used to collect average spectra of 32 scans at every 2^{nd} wavelength from 1100 nm to 2498 nm. Furthermore, 2-D NIR spectra were recorded by using a SisuCHEMA shortwave infrared line scan imaging system (Specim Ltd, Oulu, Finland). The 2-D NIR imaging system was equipped with an HgCdTe detector and the setup provided 239 absorbance values from 1000–2500 nm with a 6.3 nm spacing. A typical image size of the acquired hypercubes was 320x1000x239.

The X-ray absorption measurements performed for the studies described in Paper IV and V were conducted at the I811 beamline (Figure 7) at the MAX-Lab II synchrotron, Lund, Sweden. XANES spectra were acquired in fluorescence mode at 0.1 eV intervals over the range -50 eV to +150 eV from the K-edge of calcium (Ca) (4038.5 eV). All measurements were conducted under a helium atmosphere and five XANES spectra were acquired for

constructing mean spectra. All sample handling was conducted in a glove box flushed with helium to avoid oxidation of samples.

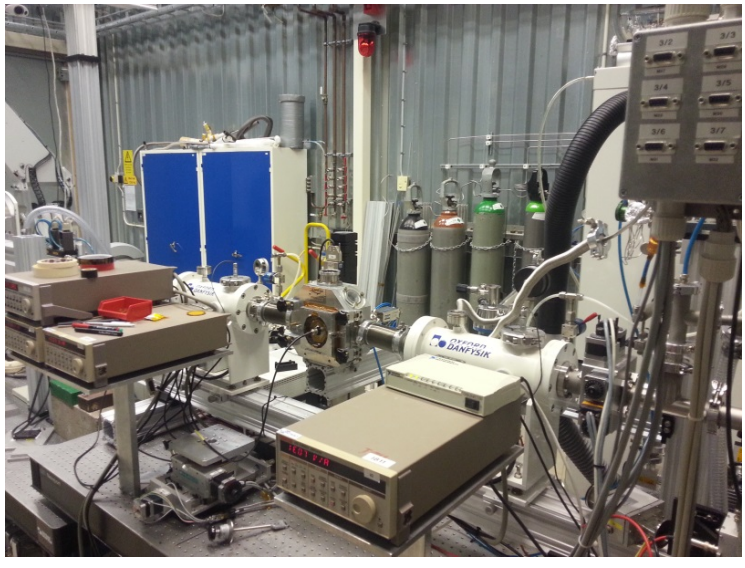

Figure 7. XAS experimental setup at the I811 end station at the synchrotron MAX Lab II.

A number of reference chemicals (see Paper IV) were ground in a mortar and mixed with $B(NO_3)_3$ for the acquisition of XANES spectra of probable phases present in the thermally treated samples. Some of the reference chemicals were synthesized, i.e., fairchildite ($K_2Ca(CO_3)_2$), and $K_2Ca_2(CO_3)_3$ according to Navrotsky *et al.* (1997), and hydroxyapatite ($Ca_5(PO_4)_3)_2(OH)$) according to PhD. Nils Skoglund (pers. com. June 2014) through solid phase reactions at 450–800 °C. Synthesized reference chemicals were verified by powder X-ray diffraction using a Bruker AXS d8 Advance diffractometer housed at the Tech-Lab, Umeå University, Umeå, Sweden.

The STXM imaging presented in Paper V was conducted at the Canadian Light Source (CLS) synchrotron located in Saskatoon, Saskatchewan, Canada. The thermally treated microtome sections were examined by light microscopy (Figure 8a) to find suitable regions of interest (ROIs). Thermally untreated sections were also examined (labelled RCG60). The sections were subsequently transferred to the STXM instrument (Figure 8b) and a quick "on-off" map of the ROI was obtained by scanning a pre-edge energy and the tabulated edge energy of carbon and calcium, respectively. If the on-off map analysis was satisfactory, an imaging stack dataset was collected of the ROI in transmission mode under a helium atmosphere.

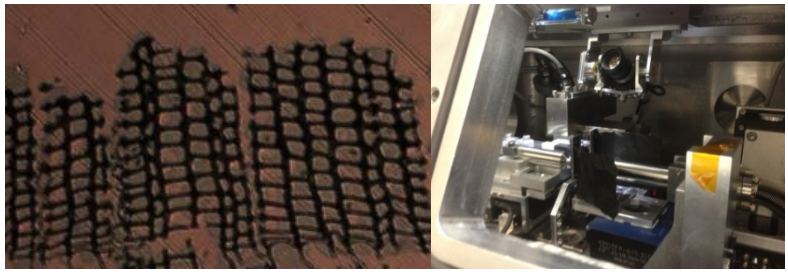

Figure 8. (left) Light microscope image of RCG thermally treated at 300 °C, (right) photograph of the synchrotron STXM at the Canadian Light Source (CLS), Saskatoon, Canada.

For the carbon and calcium measurements, the regions 280–305 eV and 344–360 eV region were used, respectively. Typical image stack sizes were 120×120×94.

FT-IR spectroscopy was used to gather additional information on the carbon matrix of the thermally treated and untreated RCG samples in the study presented in Paper V. Powder samples were mixed with KBr (infrared spectroscopy grade, Fisher Scientific, UK) and analysed using a Bruker IFS 66 v/S spectrometer under vacuum (4 mbar) with a standard DTGS detector. Manually ground KBR was used as background. Spectra were collected in diffuse reflectance mode and 128 interferograms were co-added to obtain a high signal-to-noise ratio. Spectra were recorded over the region of 400–5200 cm^{-1} with a 2 cm^{-1} spacing. For Fourier transformation, the Blackman-Harris 3-term apodization function and a zero filling factor of 2 were used. Baseline correction was conducted using 64-point rubber band correction (OPUS (version 7.0, Bruker Optik GmbH).

2.3 Modelling and software

PCA was essentially the workhorse technique for the work presented in this thesis as it was employed to analyse the data in all papers. It was not always the final evaluation method but was extensively used for overviewing the data to find boundaries, groupings, etc. Prior to all PCA analyses, the data were mean-centred column-wise according to eq. 15:

$$\mathbf{X}_{mc} = \mathbf{X\text{-}1}(\mathbf{1X}\, I^{-1}) \qquad \text{(eq. 15)}$$

Another spectral transformation that is frequently applied prior to PCA is the SNV transformation, which was used for the studies described in Paper II and V. When using standard normal variates (SNV) according to Barnes et al.

(1989), row-wise autoscaling is carried out on the transposed matrix **X** with dimension *I* rows (observations) and *K* columns of, e.g., spectral values, i.e., autoscaling is performed on $\mathbf{X}^T$. This implies that autoscaling of observations is calculated, firstly, by row-wise mean centring and, secondly, setting the variation among observations to unit variance by row-wise dividing the mean centred values by their standard deviation. If, we assume that $\mathbf{S}^T$ is the row-wise mean centred matrix of $\mathbf{X}^T$, then SNV is calculated in matrix notation as

$$\mathbf{X}^T_{SNV} = \mathbf{S}^T[\mathrm{diag}[(K\text{-}1)^{-1}\mathrm{diag}(\mathbf{S}\mathbf{S}^T)]^{1/2}]^{-1} \qquad \text{(eq. 16)}$$

For PCA analysis, the following software were used: Matlab (The MathWorks Inc., Natick, MA. USA) , PLS_Toolbox (Eigenvector Res. Inc., Wenatchee, WA, USA), SIMCA 13.0 (Umetrics, Umeå, Sweden) and Evince (Umbio AB, Umeå Sweden).

For the PLS regression reported in Paper I and III, Matlab and PLS Toolbox was used exclusively. The variable selection employed in Paper I was based on VIP scores (Wold, 1994) and interval PLS (iPLS) (Norgaard *et al.*, 2000) was conducted using PLS Toolbox.

In work described in Paper IV, the conversion of raw data to $\mu(E)$, energy calibration, aligning and merging of spectra, pre and post edge spline fitting and normalization were conducted using Athena 0.8.061 (©2001–2009, Bruce Ravel) (Ravel & Newville, 2005). The analysis of XANES spectra mainly consisted of linear combination fitting (LCF) of sample spectra to reference compound spectra, also performed in Athena. In LCF, the algorithm tries to fit the unknown spectra to spectra from reference compounds in a least square sense to minimize the residual.

In the study for Paper V, the software Axis2000 (A. Hitchcock, McMaster University, Hamilton, Canada; built on IDL software, Research Systems Inc., Boulder, Colorado) was used to analyse the on-off maps for carbon (C 1s; K-edge) and calcium (Ca 2p; L-edge) in order to determine suitable ROIs. On-off maps were constructed by acquiring one stack at a pre edge energy and another at a post edge energy with maximal absorption and subsequently subtracting the pre edge map from the post edge map. Selected ROIs were scanned across the absorption edges and individual energy maps were stacked using the software Stack_Analyze (C. Jacobsen, SUNY Stony Brook; built on IDL software, Research Systems Inc., Boulder, Colorado). Maps were aligned using the 290 and 353 eV map as reference for the carbon and Ca stacks, respectively. For each stack, one empty area, which did not contain any cell wall material, and thus had low absorption, was chosen for background correction (I_0). The stacks were then converted to optical density (OD). PCA

was performed on individual stacks using the program PCA_GUI 1.1.1 (Lerotic *et al.*, 2004).

For the construction of mosaic images, individual maps were saved as tiff files in Stack_Analyze, imported into MATLAB and reconstructed into hypercubes ($x \times y \times z$) with the original dimensions. Since some hypercubes had misaligned maps with regard to energy, a MATLAB script was written to identify the correct and misaligned energy maps. The next step was to perform a pixel-wise calculation by fitting a linear polynomial function between the two closest adjacent correct maps and then predict the optical density pixel-wise at the appropriate energy. After recalculating the predicted maps, the hypercubes were reconstructed with the appropriate energy scale and equal size in the *z*-dimension, and finally, an OD mask was applied, discarding all pixels that had OD values > 1.5. The merging of individual stacks to produce the mosaic images and subsequent PCA analysis were carried out using Evince.

3 Results and discussion

In the following section the characterization of the lignocellulosic materials used in the thesis is divided into, firstly, the study of the organic matrix by the used spectroscopic methods, and secondly, the study of ash content and inorganic elements, especially calcium.

3.1 Characterization of the organic matrix of biomass

3.1.1 2-D NIR for separation of wood chips

Biomass shows large heterogeneity with regard to organic matrices, as well as inorganic compositions between different kinds of biomass assortments (Vassilev *et al.*, 2010; Vassilev *et al.*, 2013a). Moreover, inter-species variation can be substantial, one example being the extractive content in woody biomass. Several softwood species, such as Scots pine (*Pinus sylvestris* L.), form sapwood and heartwood that have different inherent amounts of extractives. The higher extractive content in heartwood has largely been explained by the large numbers of ray and parenchyma cells (Esteban *et al.*, 2005).

Moreover, as trees grow, firstly juvenile wood successively develops radially outwards from the pith (the first 10-20 year rings) then followed by mature wood, and it is common to classify wood as either mature or juvenile wood. It has been shown that the mature and juvenile heartwood of the black locust (*Robinia pesudoacacia* L.) differ significantly in extractive content, especially phenolic compounds and flavonoids (Dunisch *et al.*, 2010). Consequently, a tree consists of several classes based on extractive content. In Paper II, the use of 2-D NIR spectroscopy for classifying different wood classes and identifying wood chips with elevated levels of extractives is reported. PCA analysis was conducted on four hyperspectral images of pine wood chips that had been divided into four classes: mature and juvenile sapwood, and mature and juvenile heartwood. The PCA score plot (Figure 2 in

Paper II) indicated three clusters: heartwood and sapwood were readily separated and separation between juvenile and mature sapwood was also obtained. By studying the loadings of PC1 (mainly separating sapwood and heartwood), it was concluded that wavelengths corresponding to water binding were responsible for the separation.

An additional PCA was conducted on a constructed mosaic consisting of NIR images of pine juvenile and mature sapwood, pine mature heartwood and pine knot wood. The distribution of extractives in the knot wood chip material was expected to be heterogeneously distributed because this class comprised of a mixture of juvenile and mature sapwood with relatively low extractive content and knot wood with reportedly higher extractive content (Boutelje, 1966). The results of the corresponding PCA are presented in Figure 4 in Paper II, which shows the score values of the second PC plotted as pixel values in the original image.

Pine knot wood was clearly separated from the other types of wood chips in PC2, which explained 23.5 % of the variation in the data. Red areas in the pine knot wood image (denoted PK) were hypothesized as areas that were highly enriched in extractives. Interpretation of the loadings of PC2 as well as pixel spectra (Figure 9A), extracted from a separate PCA performed solely on knot wood (shown in Figure 9A), indicated regions in the NIR spectra that corresponded to CH, CH_2, CH_3 and CH=CH in extractives (Westad *et al.*, 2008).

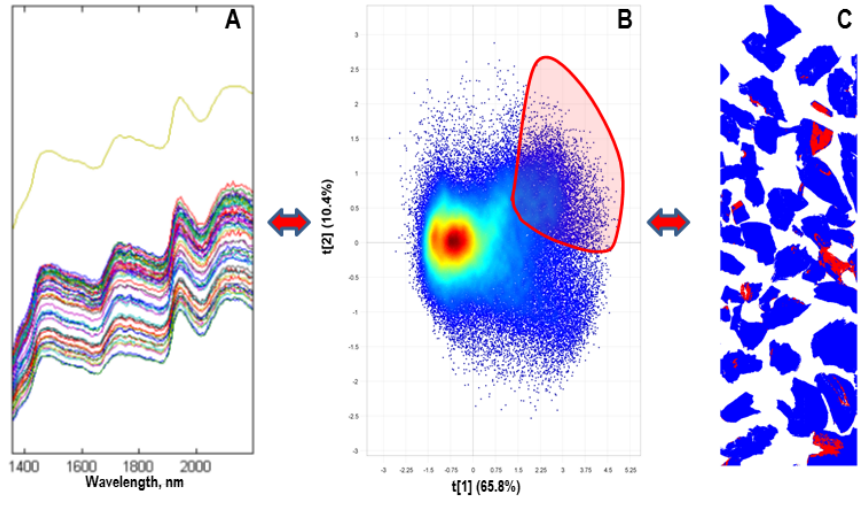

Figure 9. PCA model results for 2D-NIR image of pine knot wood: (A) NIR spectra of selected pixels with the mean spectra (yellow) plotted atop; (B) score plot of the first and second component; and (C) false colour image of chips on a conveyer belt, with selected pixels from the score plot marked in red.

Figure 9 also showcases the usefulness of modern multivariate image analysis (MIA) software, by which the user can examine groups of pixels, e.g., in a score plot (9B), identify the spatial location in the image (9C) and, finally, extract spectral information (9A) needed for chemistry evaluation.

To further confirm the findings from the second PCA model, a PLS constructed from a 1-D instrument was used to predict extractive content in individual pixels. The results from the PLS prediction (Figure 7, Paper I), showed close resemblance to the PC2 score plot of the second PCA (Fig 4, Paper I). The PLS regression models also enabled more precise study of the wavelength importance on the projection. By studying the regression coefficient plot of the image PLS model, peaks corresponding to C-H bonds were identified (at 1212 nm, 1346 nm, 1723–1764 nm and 2320 nm).

In conclusion, the work presented in Paper I showed that 2-D NIR spectroscopy is a viable technique for identifying pine wood chips by extractive content. For exact determination of the extractive levels in individual chips, further work is needed to build specific PLS models based on pieces of individual wood chips.

3.1.2 Carbon transformation in thermally treated RCG cell walls.

Investigation into the effect of torrefaction and pyrolysis treatment of microtome sections of RCG in order to study thermal decomposition of cell wall polysaccharides was conducted using synchrotron-based STXM C 1s NEXAFS spectroscopy and is presented in Paper V. STXM is a microscopy technique that uses highly focused X-rays in the 25–40 nm range to construct individual images at energies around absorption edges of the element of interest, thus yielding an X-ray absorption spectrum in each pixel.

The thermal treatment of RCG sections, which was conducted at 90, 300, 400 and 500 °C under a N_2 atmosphere, was expected to have a large impact on the cell wall structures and chemistry. In general, resonances from hydrogen and oxygen functional groups of carbon decreased substantially as the temperature was increased. A PCA of a mosaic image was performed, from which five groups were identified based on their position in the PCA score plot. Identified group spectra were extracted and compared to reference standards from cell wall matrix elements, such as cellulose, hemicelluloses and lignin, allowing the thermal decomposition of the cell wall to be established, as summarized in Table 3.

Additionally, FT-IR spectroscopy on thermotreated RCG powder was also conducted in order to further elucidate the thermal decomposition of RCG under an N_2 atmosphere (Table 3).

Table 3. Assignment of C 1s NEXAFS and FT-IR spectral peaks for thermally treated RCG sections and powders. Temperature is defined as the temperature where major transition occurred in the spectra and origin is the likely C species where the transition/vibration occurred. Italic text indicates an increase in signal, whereas normal text indicates a decrease. Cellulose, hemicellulose and lignin are denoted Cell, Hemi, Lig, respectively. S: stretching, .A: asymmetric stretching and B: bending.

Ca 1 s NEXAFS Peak energy (eV)	Transition	Temperature (°C)	Origin
284.3	*C=C, 1s-π**	*400-500*	*Quinone*
285.3	C=C, 1s-π*	300-400	Lig
287.0	C-O, 1s-3p/σ*	200-400	Lig/Hemi
	C-H, 1s-π*	200-400	Lig
289.0	C-O, 1s-3p/σ*	300-400	Cell/Hemi/Cell
290.7	Unresolved	-	-

FT-IR Wavenumber (cm^{-1})	Vibration		
3320	O-H (S)	300-400	Lig/Hemi/Cell
3045	*C-H (S)*	*300-500*	*Lig*
2924	C-H (S)	300-500	Hemi
1710	C=O (S)	300-400	Lig
1593	*C=C (A)*	*300-400*	*Lig*
1514	C=C (A)	300-400	Lig
1240	C-O (S)	90-300	Hemi
1110	C-O-C (S)	300-400	Hemi
1065	C-O/C-H (S)	90-400	Hemi
	C-OH (B)	90-400	Hemi
905	C-H (B)	300-400	Cell
810	*C-H (B)*	*300-400*	*Lig*
465	Unresolved	-	-

Peak assignments were made according to (Francis & Hitchcock, 1992; Bustin & Guo, 1999; Sun *et al.*, 2000; Xiao *et al.*, 2001; di Stasio & Braun, 2005; Cody *et al.*, 2009).

Minor changes in the C 1s and FT-IR spectra were observed when comparing RCG treated at 90 °C and 300 °C. The most obvious change, although small, was a reduction of the signal in the 287.0 eV region of the C 1s NEXAFS spectra of RCG treated at 300 °C (Figure 3 in Paper V).

This region corresponded to C-O and C-H in lignin and hemicellulose, respectively (Table 3), which suggests that the small decrease is probably due to minor degradation of hemicelluloses, as has previously been reported at temperatures between 200–350 °C (Bridgeman *et al.*, 2008). The reduction of the peak at about 1240 cm^{-1} in the FT-IR spectra, which corresponds to C-O stretching in hemicellulose, further confirms this interpretation. When comparing the 300 °C treated RCG sample with that treated at 400 °C, major changes were detected in both the C 1s and FT-IR spectra, implying that between 300–400 °C, major degradation of the cell wall polymers occurred.

In the STXM spectra recorded after treatment at 400 °C, a significant reduction of the C-O resonances at about 289.0 eV occurred, which indicates major decomposition of cellulose and hemicellulose (Table 3). The signal due to C=C resonances in lignin was also slightly reduced, in line with the reported broad degradation temperature of lignin between 200–500 °C (Brebu & Vasile, 2010). The FT-IR measurements also confirmed this, as all cellulose, hemicellulose and some lignin assigned peaks in the FT-IR spectra declined between 300–400 °C.

At 500 °C, drastic changes were observed, as the structural integrity of the cell wall was lost (Figure 1 in Paper 5). Moreover, the resonances due to C-O were absent in the C 1s NEXAFS spectra and a sharp increase in the signal at 284.3 eV, corresponding to aromatic C=C bonds in quinines, was observed. These spectra (named RCG500(2) in Figure 3 in Paper V) were acquired from a supposedly empty area in the image (no apparent structures), which suggests that this C phase was in a liquid phase during the thermal treatment. Some residual resonances were found at 287.0 eV, representing C-H from lignin. The FT-IR spectra corroborated the results from the C 1s NEXAFS experiment by showing increased intensities from aromatic vibration, e.g., at 3045 and 810 cm^{-1}.

In conclusion, analysing STXM C 1s NEXAFS images with a global mosaic PCA allowed pixel group identification, making extraction of the relevant pixel spectra relatively straightforward. Subsequent analysis of extracted spectra showed that thermal degradation of the cell wall mainly occurred between 300–500 °C with substantial loss of oxygen and hydrogen functional groups. At 500 °C, aromaticity increased, in agreement with Yaman (2004), who found that thermal decomposition of biomass above 400 °C is an aromatization process, whereas at lower temperatures, it is classified as a degradation process. FT-IR is a powerful method for examining the organic components of biomass, but it lacks spatial resolution if imaging is desired due to wavelength limitations.

3.2 Characterization of inorganic elements in biomass

3.2.1 XRF and NIR characterization of biomass

The viability of using XRF spectroscopy and multivariate statistical methods, such as PCA and PLS, to assess the inorganic components and total ash content in a variety of biomaterials was tested in the study upon which Paper 1 is based. The studied biomaterials were of different type and origin (stem wood, herbaceous and agricultural residues) and were chosen in order to test the boundaries of the constructed calibration models. In a real case scenario, such as at the gates of a biorefinery, an arsenal of broad calibration models that accurately can predict origin, type and elemental composition of an incoming feedstock could be highly valuable. The elemental compositions, as measured by wet chemical methods (ICP-MS and ash content analysis), are shown in Table 4 as mean values for the different types of biomass studied.

Table 4. Elemental composition and ash content of biomaterials studied in the work described in Paper I. The hemp samples were divided into two categories depending on harvest time (fall or spring). Mean values presented are in % of dry weight.

Samples	Ash	Al	Na	Mg	P	Si	K	Ca
Wood	0.34	0.00	0.00	0.01	0.00	0.02	0.04	0.07
Hemp-fa.	8.31	0.01	0.01	0.15	0.23	0.25	0.68	1.13
Hemp-sp.	2.48	0.02	0.01	0.05	0.09	0.14	0.10	0.65
Grape res	7.61	0.07	0.05	0.07	0.04	0.63	0.85	0.57
Olive res	7.17	0.02	0.03	0.13	0.23	0.10	2.16	0.81

The different biomass types showed great heterogeneity among groups, especially hemp, which also showed great variation within the group, depending on harvest time. Spring harvested hemp had significantly lower total ash content and potassium content (the latter by a factor of seven), compared to that harvested in the fall. The delayed spring harvest technique has been shown to significantly reduce the inorganic content of herbaceous material due to leaching during winter (Burvall, 1997; Xiong *et al.*, 2009).

In the work described in Paper I, a clear separation of the studied biomaterials was obtained by using PCA on XRF spectral data. The PCA model shoved that fall harvested hemp exhibited the largest spectral variation. By studying the loadings of the PCA model, it was shown that the potassium and calcium regions of the XRF spectra (3.31 and 3.69 keV, respectively) were the most influential regions of the XRF spectra for PC1 and PC2, respectively. The results of the corresponding PCA model conducted on sample reference

data from ICP-MS analyses are presented as a score plot of the first and second component (Figure 10).

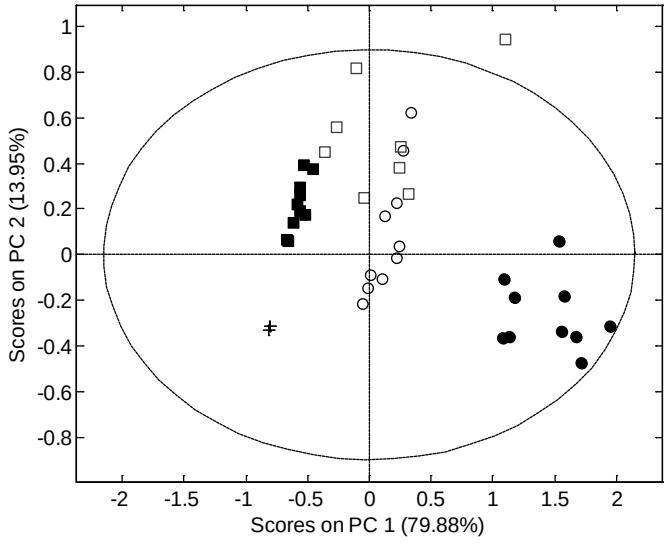

Figure 10. PCA score plot of the first and second principal component from ICP-MS data of stem wood (+); hemp harvested in spring (■); hemp harvested in fall (□); grape residues (●); and olive residues (○).

This PCA score plot is similar to the one obtained by performing PCA on XRF spectral data reported in Paper I, with one exception: the group of hemp samples that were fall harvested was shifted in position towards PC2 and also showed low score value variation in PC1. This implies that the fall harvested hemp samples showed an enhanced potassium signal in the XRF spectra. The most likely candidate for this is fluorescence from Ca, which shows a K_{α} line at 3.69 keV, and therefore is particularly well suited toward exciting inner-core electrons of K, which has an inner-core electron binding energy of 3.61 keV (Williams, 2009). Thus, a plausible explanation for the unexpected and relative large prediction errors of both Ca and K PLS calibration models constructed in Paper I is confounding matrix effects due to enhancement.

3.2.2 PLS calibration modelling of ash elements and content

In Paper I and III, multivariate statistical calibration models using PLS are described for the total ash content and in Paper I for the elemental composition of biomass of different varieties. In the study reported in Paper 1, the calibration models for specific ash elements were evaluated by calculating

diagnostic parameters described in section 1.9.3 of this thesis. One especially important diagnostic tool was *RMSEP*, which was not only used to evaluate the predictive ability of the model but also to choose the appropriate number of PLS components as the first local minimum. The results from the constructed PLS calibration models of single ash elements are shown in Figure 11 and presented as *RPD* (see section 1.9.3).

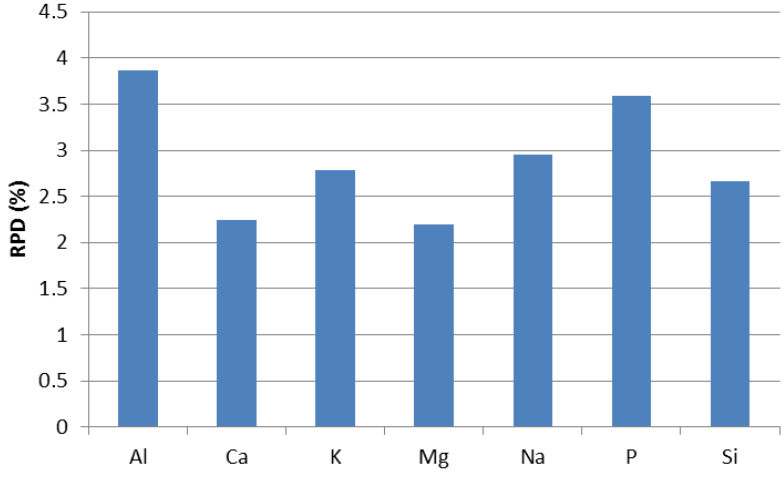

Figure 11. RPD values of constructed calibration models for single ash elements.

The performance of the constructed PLS models were evaluated according to the classification of Saeys *et al.* (2005). The models for Ca and Mg were classified as having approximate quantitative predictability, the models for K, Na and Si were classified as having good predictability and the models for P and Al were classified as having excellent predictability. The relatively poor performance of the Ca and K calibration models, despite having large and distinct K_α peaks in the XRF spectra, could either be explained by matrix effects, as discussed earlier, or the calibration models being too broad.

When using spectral data, such as the data obtained from the XRF instrument used in the study of Paper I, a spectrum consists of over 2300 variables (bins; 15 eV in each bin), which often leads to PLS model inclusion of parts of the spectra that make a low contribution to the PLS projection. This may lead to PLS models with impaired predictive capabilities. Furthermore, if computational speed is an issue it is often desirable to reduce the matrix size. This was tested in the work described in Paper I by using two different methods of variable selection, i.e., interval PLS and VIP selection. Both methods reduced the matrix size by approximately 95 % and in several cases

improved the *RPD* value of the PLS calibration model. The results of one iPLS model for potassium are presented in Figure 12, which provides an example of how iPLS variable selection may affect the calibration model, yielding lower prediction errors.

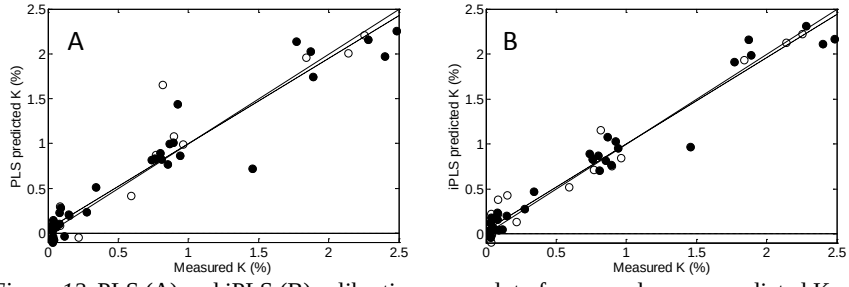

Figure 12. PLS (A) and iPLS (B) calibration score plot of measured versus predicted K content in the biomass samples used in the study described in Paper I. Filled circles represent samples in the calibration set, whereas open circles represent samples in the test set. The solid line represents a perfect fit, whereas the dashed line represents the actual fit of the test set.

The *RMSEP* values were 0.26 and 0.16 % for the PLS and iPLS calibration models depicted in Figure 12, respectively, demonstrating that iPLS variable selection can improve a PLS model. However, in the study of Paper I we examined the concept of repeated measurement and several of the variable selected VIP and iPLS models had large error values related to precision. This implies that caution should be exercised when variable selection is used and the selected spectral regions should be evaluated in order to ensure that modelling of noise that co-varies with the response is avoided. Moreover, relative errors of prediction (*REP*) were calculated and found reasonable.

In the studies of Paper I and III, XRF calibration models of ash content were successfully constructed with excellent predictive capabilities, which has important practical implications as ash content often can be used as an indicator of fuel quality. If ash content is high and relative concentrations of, e.g., potassium, sodium, calcium, silica, etc. are unfavourable in the fuel, the risk of operational disturbances such as slagging and fouling increases (Bostrom *et al.*, 2012). The size of combustion applications is also important when considering the effect of ash content. In residential combustion applications, such as pellet burners, high ash content often leads to increased maintenance and operational shutdowns (Obernberger & Thek, 2004)

XRF and NIR spectroscopy was used in the work described in Paper III to evaluate the performance of each method in determining the ash content of 119

samples (ash content between 0.2–5.7 %, d.w.) collected at Swedish combined and heat power (CHP) plants. NIR spectroscopy, with a proven ability for measuring moisture content in wood (Lestander *et al.*, 2012), has been shown to be a suitable technique for measuring inorganic components in biomaterials (Clark *et al.*, 1987; Huang *et al.*, 2009; Bruun *et al.*, 2010) as well as ash content (Lestander & Rhen, 2005) by indirect associations between organic matrix and ash elements. To test this, separate PLS calibration models were constructed for XRF and NIR. Twenty samples were exogenously contaminated and predicted using the constructed PLS calibration models in order to study the capacity of each technique for measuring contaminants in biomass samples. The results are shown in Figure 13.

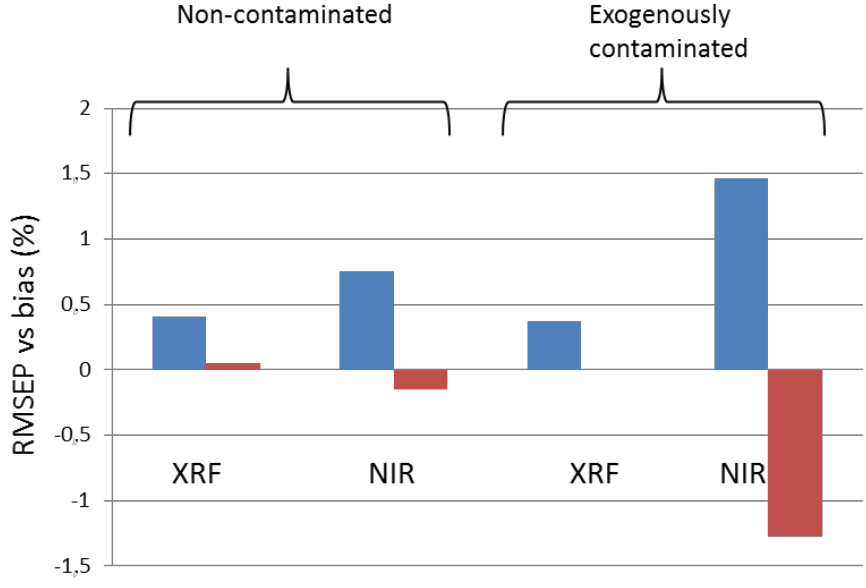

Figure 13. RMSEP (blue bars) and bias (red bars) obtained from PLS calibration models constructed from XRF and NIR spectra when used to predict biomass samples from CHP plants with and without exogenous contaminants .

XRF spectroscopy showed substantially lower prediction errors compared to NIR spectroscopy, especially for the exogenously contaminated samples (XRF showed a bias close to zero in both cases), as shown in Figure 13. The bias of the NIR model for the contaminated samples was largely negative; indicating that this calibration model clearly under-estimated contaminated samples. This result suggests that the NIR technique may fail to identify ash, especially non-embedded inorganic elements, resulting in large prediction errors in total ash content if the ash elements are not associated with the organic matrix.

However, if NIR and XRF are used in conjunction, additional information can be gleaned. Figure 14 shows the prediction residuals of the XRF and NIR calibration models versus the amounts of added ash elements in the contaminated samples.

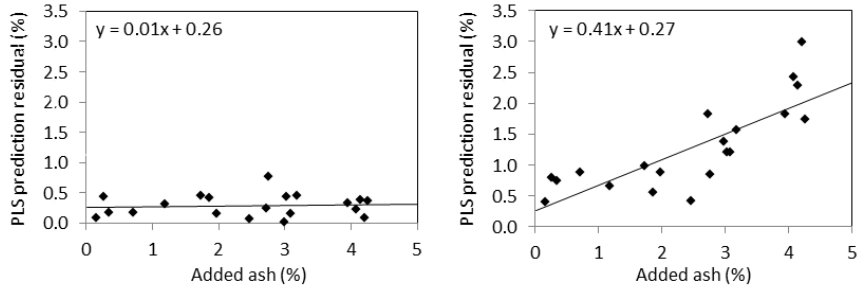

Figure 14. Prediction residual of XRF (left) and NIR (right) calibration models versus the amounts of added ash elements in the contaminated samples. N.B. The prediction residuals are expressed as absolute values.

The clear connection between the added ash elements and prediction residual of the NIR model (Figure 14 (right)) suggests that by comparing individual discrepancies between sample predictions of XRF and NIR, it may be possible to elucidate whether the ash elements are organically embedded or not. In conclusion, if high precision is needed for ash content determination, XRF is the best method. However, if only relative ash content levels are required, NIR could be a viable technique. If both techniques are used in conjunction, more information can be gained, e.g., regarding the degree of contamination contributing to the ash content in biomass.

3.3 X-ray absorption spectroscopy of calcium

3.3.1 Ca speciation in thermally treated pine at low oxygen partial pressures

In the work described in Paper IV, Ca phase transitions at low oxygen partial pressures were studied on thermally treated Scots pine samples by XANES spectroscopy. Thermodynamic equilibrium calculations based on chemical composition, N_2 atmosphere and temperatures ranging from 100–800 °C were conducted using thermodynamic data taken from the Factsage database version 6.4 (Bale *et al.*, 2002). The results from the thermodynamic modelling are shown in Figure 15.

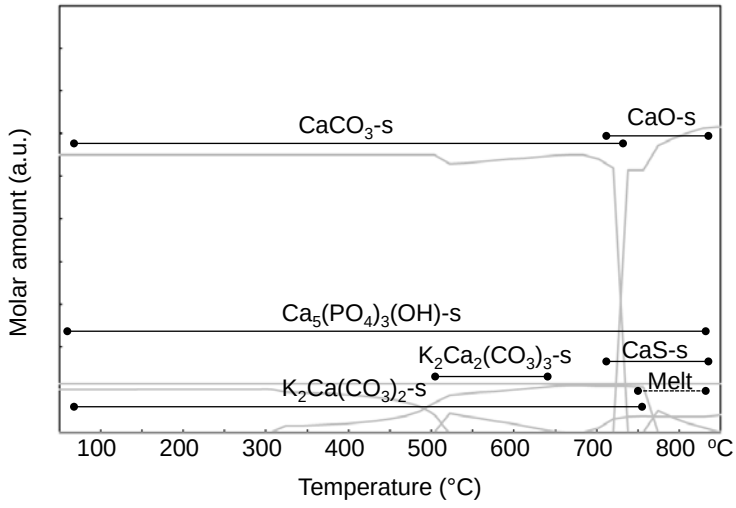

Figure 15. Distribution of calcium between condensed phases based on chemical equilibrium analysis for wood under an N_2 atmosphere as a function of temperature.

The results from the thermodynamic equilibrium modelling indicate that the carbonate system dominated the thermal decomposition of Scots pine powder. At the lowest temperatures, calcite ($CaCO_3$) and hydroxyapatite ($Ca_5(PO_4)_3OH$) were predicted to be the dominant phases. Conversely, at higher temperatures, calcium oxide (CaO), hydroxyapatite and calcium sulphide (CaS) were the prevalent forms. Fairchildiite ($K_2Ca(CO_3)_2$) and $K_2Ca_2(CO_3)_3$ were predicted as an intermediate phase over the temperature range 100–600 °C.

The data presented in Paper IV was overviewed by constructing a PCA of XANES sample spectra. The samples ranging from untreated to the 600 °C treatment were distributed along the first PC, whereas the 800 °C treated samples lay along the second PC (Figure 2a in Paper IV). To make a first assessment of which reference chemicals to use in the LCF analysis, XANES spectra of reference chemicals were predicted by the PCA model and the results are shown in Figure 2b in Paper IV. Selected reference chemicals were subsequently used for LCF analysis of the 24 thermotreated samples plus one untreated sample (Figure 16). The results from the LCF analysis of XANES spectra of thermotreated pine powder clearly show that Ca oxalate was the most prevalent phase in untreated pine (Figure 16a), but as temperature was increased, the amount of oxalate decreased almost linearly. This indicates a decomposition reaction that increases in rate with increasing temperature. The expected decomposition product of Ca oxalate was $CaCO_3$, which was found in small amounts in pine powder thermotreated at 300 °C but then increased

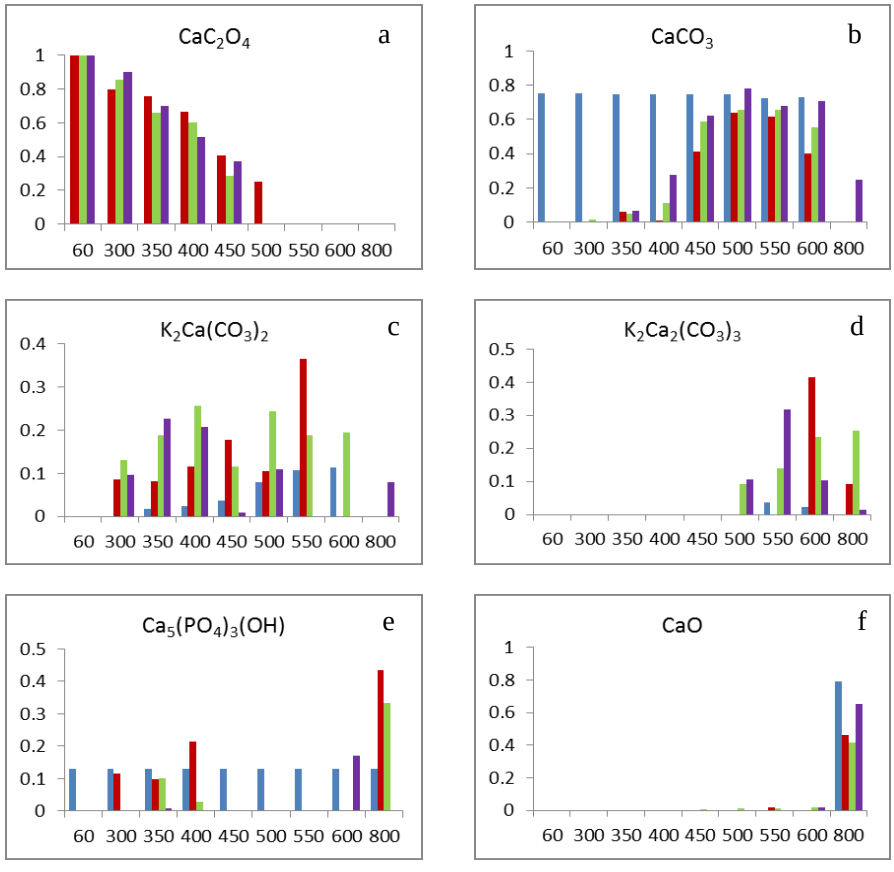

Figure 16. Ca phases in pine powder thermotreated at 60–800 °C as predicted by LCF analysis expressed as proportions. Blue bars indicate thermodynamic equilibrium predictions, red bars indicate N_2, green bars indicate 3 % O_2 and purple bars indicate 6 % O_2 atmosphere for (a) CaC_2O_4, (b) $CaCO_3$, (c) $K_2Ca(CO_3)_2$, (d) $K_2Ca_2(CO_3)_3$, (e) $Ca_5(PO_4)_3(OH)$, and (f) CaO.

proportionally up to 500 °C, after which it slightly decreased (Fig 16b). As Ca oxalate was considered unstable under the conditions used in the experiments, it was excluded from the thermodynamic equilibrium models. The models instead predicted high values of the decomposition product of Ca oxalate, i.e., $CaCO_3$, even though the experimental XANES data for the low temperature treatments clearly showed that Ca oxalate is the primary Ca phase. This disparity indicates that the system was not in equilibrium, which is not surprising since solid phase reactions are generally slow, especially at low temperatures. Thus, the 600 s experimental period of the thermotreatment was probably too short for reaching equilibrium states.

At 300 °C, the LCF analysis of XANES spectra predicted that Ca-K-carbonates started to form (Figure 16c). This is a somewhat lower temperature

than previously reported. Navrotsky *et al.* (1997) used 480 °C in order to synthesize the low temperature polymorph of $K_2Ca(CO_3)_2$, butscheliite. In the present study of pine powder, the formation temperature appeared to be lower. This might be a consequence of decomposition reactions of wood matrix elements, producing CO and CO_2 gas that may trigger inorganic reactions at lower temperatures. The same trends were observed for the formation of $K_2Ca_2(CO_3)_3$ (Figure 16d), which started to form around 500 °C, in contrast to the synthesis temperature of 750 °C used by Navrotsky *et al.* (1997). The origin of the potassium present in the Ca-K-carbonates is unknown.

The thermodynamic equilibrium model predicted that hydroxyapatite ($Ca_5(PO_4)_3(OH)$) should be stable and present at all treatment temperatures. The LCF analysis of the XANES data found hydroxyapatite in two temperature regions: at around 300-400 °C and at 800 °C. The low temperature region is probably too low for formation of hydroxyapatite. These confounding results cannot be explained within the context of this thesis, and thus further studies are required. Moreover, no experiments on Ca-P formation at reducing conditions were found in the literature.

In conclusion, XANES spectroscopy seems to be a viable method for describing complex systems that have several phases present in the same samples, such as Ca phase transitions in biomass. The results obtained in this study demonstrate the usefulness of this technique.

3.3.2 Ca nano-mapping by STXM

Calcium nano-mapping was conducted by using synchrotron-based STXM and is presented in Paper V. Calcium crystals of various sizes were mostly found lining the walls of xylem cells in the RCG sections. An example of Ca localization is presented in Figure 17. Calcium nano-mapping was conducted using the on-off mapping technique, in which maps were acquired at pre-edge and at-edge energies, in this case at 345 and 352.9 eV, yielding two maps, one low and one high in absorption. Next, the pre-edge map (low energy) was subtracted from the at-edge map (higher energy) and the resulting map consists of pure Ca signal. False colour images are often constructed for visualization, where one layer represents the calculated on-off map and the remaining layer represent the pre-edge energy map. When studying Figure 17b, large and small crystals were identified by visual inspection. To determine Ca crystal sizes, the image was imported to ImageJ (Schneider *et al.*, 2012).

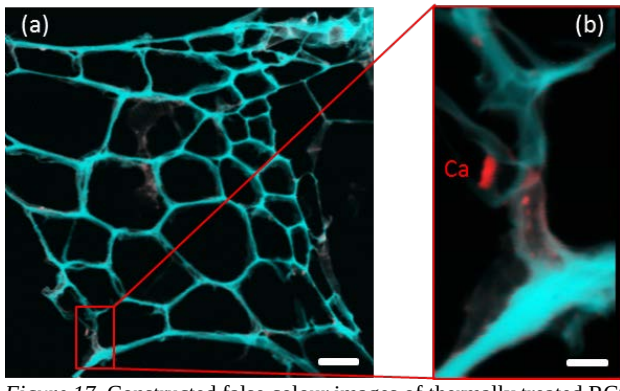

Figure 17. Constructed false colour images of thermally treated RCG at 400 °C collected as on-off Ca maps at 345.0/352.9 eV with image sizes of (a) 50×50 µm, scale bar = 5 µm, and (b) 5×10 µm, scale bar = 1 µm. Red colour indicates Ca and green the C matrix of the cell wall.

Prior to Ca particle measurement, the image was split and thresholded to remove noisy pixels with low Ca intensity. Particle measurement results are shown in Figure 6 in Paper V. The particle distribution was found to be shifted towards ultra-fine particles; approximately 50 % of the detected Ca crystals were found to have particle sizes of < 100 nm. This result might shed some new light on the findings of Wu *et al.* (2011), who showed the presence of Ca submicron particles during the combustion of flue gas of coal and waste derived fuels. Ca is generally not volatilized during combustion and is considered refractory, often found in bottom-ashes. Our findings suggest that Ca ultrafine particles have sufficient small sizes to be mobile in combustion processes and are possibly transported in flue gases associated with char particles or as solitary ultrafine particles. The primary Ca phase of RCG was found to be Ca oxalate (CaC_2O_4). In conclusion, STXM offers possibilities for studying complex systems, such as the determination of Ca crystal localization at cell walls at nanometer scale and calculation of the size distribution of such crystals.

4 Conclusions

The following list summarizes the main conclusions in this thesis:

- 2-D NIR spectroscopy is a viable technique for classifying different wood classes and identifying wood chips by extractive content. Furthermore, heartwood and sapwood were separated and separation between juvenile and mature sapwood was also obtained.
- XRF spectroscopy can readily be used for accurate classification of different kinds of biomass materials with regard to inorganic composition by using multivariate methods such as PCA.
- PLS calibration models based on XRF spectra can be constructed with good predictive capabilities for single inorganic elements, as well as ash content in biomaterials, therefore offering potential for at-line applications in future biorefineries.
- XRF spectroscopy is a superior technique for measuring ash content in biomass materials compared to NIR spectroscopy, especially if exogenous contaminants are present in the material.
- If XRF and NIR are used in conjunction, intrinsic and exogenous ash components can be differentiated.
- Ca speciation in thermally treated pine powders at low oxygen partial pressures using Ca K-edge (1s) XANES spectroscopy and subsequent LCF analysis produced results that were in general agreement with thermodynamic model predictions.
- Ca oxalate was found by XANES spectroscopy to be the primary Ca phase in untreated pine wood, and carbonates, including Ca-K-carbonates, dominated the Ca phase transitions between 300 and 600 °C.
- Temperature induced changes to the carbon matrix of reed canary grass (RCG) cell walls were studied with STXM-based C 1s NEXAFS

spectroscopy and the decomposition was observed in both the chemical and structural domain.

- A treatment temperature of up to 300 °C had only a minor effect on the RCG cell wall chemistry, as shown by a small reduction of resonances corresponding to lignin. At 400 °C, resonances corresponding to the C-O and C-H groups of cellulose, hemicellulose and lignin declined considerably. Finally, at 500 °C, the structural integrity of the cell wall was lost and resonances from aromatic C=C bonds increased substantially.
- Calcium nano-mapping was conducted at RCG cell walls and the particle size distributions of Ca crystals were found to be mostly in the submicron range. In fact, approximately 50 % of the crystals were found to be smaller than 100 nm, which suggests that Ca found in deposits in combustion systems originate from these Ca submicron particles present in the lignocellulosic biomass.

In all, these results have laid a foundation for the utilization of advanced spectroscopic characterization techniques for lignocellulosic biomass. More research is needed though and some ideas are outlined in the section Future research.

5 Future research

5.1 Ash element characterization

Lignocellulosic feedstock characterization, e.g., by spectroscopic methods, is of importance for a number of biorefinery process routes, e.g., in torrefaction, pyrolysis or gasification. Characterization methods need to be fast, robust and applied at-line or on-line in order to be of value as a process and quality control application, offering possibilities for feedstock tailoring and downstream process optimization. In the studies described in Paper I, II and III, NIR and XFR were used to characterize organic and inorganic constituents. For instance, XRF spectra were modelled by PCA and classification based on ash element composition was able to distinguish different varieties of biomass samples, as well as quantify single ash element (and total) concentrations by PLS calibration modelling. If such an approach were combined with the software used for the work reported in Paper IV for studying thermodynamic equilibrium modelling, i.e., FactSage (Bale *et al.*, 2002) and the HSC database (Roine, 2006), ash chemistry reactions could be predicted for future use in combustion applications more or less on-line solely based on XRF spectra and multivariate statistical methods.

Another possibility is to relate the elemental composition obtained by XRF with known ternary diagrams for predicting the risk of sintering, slagging and or fouling by XRF multivariate statistics directly. Such a future R&D route is outlined in Figure 18. This would also provide tools for tailoring the inclusion of additives or addition of helpful fuels in order to mitigate combustion or thermal treatment related problems.

This platform for research would require many different competences and constitute a rather large and long-term project.

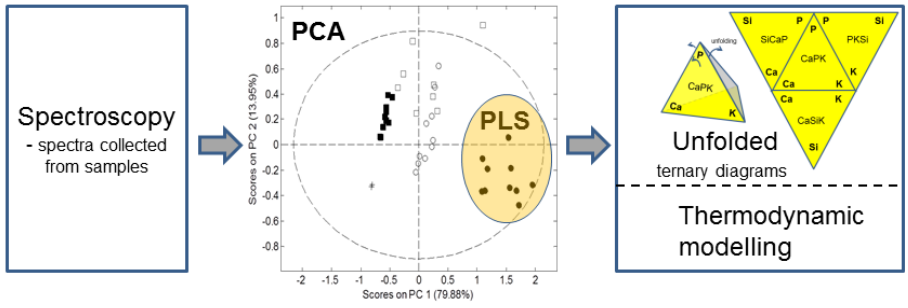

Figure 18. Outline of proposed method for monitoring and predicting ash chemistry reactions by relating spectroscopy and PCA or PLS directly to thermodynamic modelling or ternary diagrams.

Other smaller research projects include

- Comparison between laser induced breakdown spectroscopy (LIBS) and XRF spectroscopy as an on-line method for predicting ash elements. We have already initiated such research in cooperation with a research group at Idaho National Laboratory, Idaho, USA.
- In the study of Paper IV we obtained results for Ca-P phases that we were unable to explain. Therefore, further experiments are needed to explain the observed discrepancies regarding Ca-P reactions, in particular powder XRD measurements of thermotreated samples will be conducted.

5.2 Synchrotron studies

The new synchrotron MAX IV (Lund, Sweden) is currently being built and the research group has an ongoing collaboration with MAX IV managers at the SoftiMax beam line, where instrumentation for STXM is being constructed.

The following research is of specific interest:

- To examine ultrafine particles by STXM in solid recovered fuel containing biobased waste (wood, paper, cards, textiles, etc.) and deposits in convection systems based on the findings by Wu et al. to determine whether Ca is a seed source for aerosol particles.
- To contribute to the establishment of state-of-the-art phenotyping tools by using STXM for in-depth studies of wood cell structure and chemical speciation.

- To test the potential for using STXM for detailed studies during different time periods of the enzymatic saccharification of wood with modified hemicellulosic xylan and lignin connectivity.
- To use STXM in advanced studies of doped and spun nanocellulosic or lignin-based fibers to gain new knowledge for improving the production process, e.g., starting with ion liquid dissolved cellulose from chemical pulp.

To aid future research at the MAX IV and other synchrotron facilities around the world, the development of know-how is also important, i.e., in-depth knowledge of technical limitations, sample preparation, etc. for the STXM technique. This carries with it responsibility to act as coach for other researchers and industry in utilizing these advanced tools. Thus, the plans for future research to utilize these advanced infrastructures will also include plans for communication with stakeholders/end users (the first milestone in this direction was the STXM Workshop in Umeå, December 10–11, 2013, which received participation from all over the EU). In devising this platform for research and communication, it is important to involve other researchers, e.g., participating in projects like Bio4Energy and Bio4Gasification etc., but also the Research Institutes of Sweden, Swedish Forest Industries Federation, forest companies, i.e., the main protagonists behind the National Research Agenda for the forest-based industry in Sweden. Core facilities, like the advanced EM platform within the KBC research environment at Umeå University and the Swedish University of Agricultural Sciences, are also essential for this research.

Acknowledgements

Jag vill börja med att tacka finansiärerna bakom detta doktorandprojekt, Energimyndigheten och Bio4Energy. Vill även tacka MAX-Lab och CLS för stråltid.

Under mina år i den akademiska världen så har jag mött en mängd människor som har del i denna avhandling. De som har störst del är självklart mina handledare som på ett föredömligt sätt har handlett mig;

Tack Torbjörn Lestander, inte bara för den rent vetenskapliga utbildningen som du som huvudhandledare har lyckats inpränta i mig, utan även för din empati vid stunder då allt inte har gått spikrakt. Måste även passa på att tacka för ditt stora tålamod som du visat när du försökt lära mig skriva ansökningar, skriva i matrisnotation, skriva Matlab skript m.m. För övrigt är jag glad att du nästan förbjöd mig att använda Excel under mitt första år som doktorand, allt för att jag skulle lära mig Matlab. Ett verktyg som jag kommer att ha stor nytta av i resten av min forskarkarriär. Tusen tack för allt!

Tack Robert Samuelsson för att du (som biträdande handledare) alltid har tagit dig tid för mig oavsett om det handlar om vetenskapliga frågor, genomläsning av manuskript eller allmän diskussion om Sveriges senaste match i fotboll.

Tack Rainer Backman för att du (som biträdande handledare) introducerat mig till den spännande världen av förbränningskemi, tänk att Ca-speciering kan vara så intressant.

Vidare finns ett stort antal människor som hjälpt mig på olika sätt att komma dit jag är idag och er vill jag tacka;

- Stellan Marklund för att du anställde mig som diskpojke på Miljökemi och sedan gav mig möjligheten att avancera och således lära mig att elda sopor och senare upparbetning av dioxinerprover i egna projekt. Detta gav mig praktisk laboratorie vana som jag haft stor nytta av i mitt fortsatta arbete.
- Paul Geladi för att du är en aldrig sinande kunskapskälla vad gäller multivariata metoder och dina kurser är de mest värdefulla för mig som jag tagit under min doktorandtid. Vill även tacka för att du introducerade mig för hyperspektral bildanalys vilket är en synnerligen spännande teknik.
- Sylvia Larsson för att du tipsade mig om ett ledigt jobb på BTC hösten 2002. Måste vidare tacka för alla roliga projekt vi haft tillsammans och jag hoppas att det kommer bli än fler i framtiden. Tack för alla tuggummin!
- Magnus Rudolfsson för all hjälp med de termiska behandlingarna av mina prover i artikel IV och V. Men kanske mer än mer värdefullt är alla trevliga luncher och fikastunder. Det skulle inte varit lika kul på jobbet utan dig.
- Ulf Skyllberg för att du introducerade mig för synkrotronvärlden och vidare medverkat till artikel IV och V.
- Karina Thånell för Kanadaresorna och kommande resa till Schweiz, snart har jag två STXM kryss av sju möjliga. Du inspirerar mig och blir jag hälften så effektiv som du kommer jag att uträtta mycket här i livet.
- Chithra Karunakaran för att du lärt mig nästan allt jag kan om STXM NEXAFS och hjälpen med artikel V i denna avhandling.
- Lenore Johansson för all hjälp med snittning av mina prover inför STXM-resorna, vi kommer att sakna dig när du flyttar!
- Tack Håkan Örberg och Gunnar Kalén för allt praktiskt som ni har lärt mig. Trots allt damm och oväsen kommer mina minnen från BTC-tiden alltid att vara ljusa.
- Carina Jonsson för all hjälp med labb-prover och att du stått ut med att jag varit och sprungit på labbet och ibland skapat lite oreda emellanåt.
- Dan Boström och Nils Skoglund för ovärderlig hjälp med XRD analyser.
- Markus Broström för TGA analyser.
- András Gorzsás för FT-IR analyser.
- Vidare vill jag så klart tacka alla mina medarbetare på institutionen!

Slutligen vill jag tacka min älskade familj; min fru Frida, mina barn Isak och Liv för stöd och förståelse under dessa år. Nu far vi!

References

Andermann, G. & Kemp, J.W. (1958). Scattered X-rays as internal standards in X-ray emission spectroscopy. *Analytical Chemistry*, 30(8), pp. 1306-1309.

Asif, M. & Muneer, T. (2007). Energy supply, its demand and security issues for developed and emerging economies. *Renewable & Sustainable Energy Reviews*, 11(7), pp. 1388-1413.

Bale, C., Chartrand, P., Degterov, S.A., Eriksson, G., Hack, K., Ben Mahfoud, R., Melancon, J., Pelton, A.D. & Petersen, S. (2002). FactSage thermochemical software and databases. *Calphad-Computer Coupling of Phase Diagrams and Thermochemistry*, 26(2), pp. 189-228.

Barnes, R., Dhanoa, M. & Lister, S. (1989). Standard normal variate transformation and detrending of near infrared diffuse reflectance. *Applied Spectroscopy*, 43, pp. 772-777.

Beckhoff, B., Kanngießer, B., Langhoff, N., Wedell, R. & Wolff, H. (2007). *Handbook of Practical X-Ray Fluorescence Analysis*: Springer. Available from: http://www.google.se/books?id=c6d8EPYHn1EC.

Blanco, M. & Villarroya, I. (2002). NIR spectroscopy: a rapid-response analytical tool. *TrAC Trends in Analytical Chemistry*, 21(4), pp. 240-250.

Bostrom, D., Skoglund, N., Grimm, A., Boman, C., Ohman, M., Brostrom, M. & Backman, R. (2012). Ash Transformation Chemistry during Combustion of Biomass. *Energy & Fuels*, 26(1), pp. 85-93.

Boutelje, J.B. (1966). On anatomical structure moisture content density shrinkage and resin content of wood in and around knots in Swedish pine (Pinus Silvestris L) and in Swedish spruce (Picea Abies Karst). *Svensk Papperstidning-Nordisk Cellulosa*, 69(1), pp. 1-&.

Brebu, M. & Vasile, C. (2010). Thermal degradation of lignin - a review. *Cellulose Chemistry and Technology*, 44(9), pp. 353-363.

Brennan, L. & Owende, P. (2010). Biofuels from microalgae-A review of technologies for production, processing, and extractions of biofuels and co-products. *Renewable & Sustainable Energy Reviews*, 14(2), pp. 557-577.

Bridgeman, T.G., Jones, J.M., Shield, I. & Williams, P.T. (2008). Torrefaction of reed canary grass, wheat straw and willow to enhance solid fuel qualities and combustion properties. *Fuel*, 87(6), pp. 844-856.

Bridgwater, A.V., Meier, D. & Radlein, D. (1999). An overview of fast pyrolysis of biomass. *Organic Geochemistry*, 30(12), pp. 1479-1493.

Brostrom, M., Kassman, H., Helgesson, A., Berg, M., Andersson, C., Backman, R. & Nordin, A. (2007). Sulfation of corrosive alkali chlorides by ammonium sulfate in a biomass fired CFB boiler. *Fuel Processing Technology*, 88, pp. 1171-1177.

Bruun, S., Jensen, J.W., Magid, J., Lindedam, J. & Engelsen, S.B. (2010). Prediction of the degradability and ash content of wheat straw from different cultivars using near infrared spectroscopy. *Industrial Crops and Products*, 31(2), pp. 321-326.

Burvall, J. (1997). Influence of harvest time and soil type on fuel quality in reed canary grass (Phalaris arundinacea L.). *Biomass and Bioenergy*, 12(3), pp. 149-154.

Bustin, R.M. & Guo, Y. (1999). Abrupt changes (jumps) in reflectance values and chemical compositions of artificial charcoals and inertinite in coals. *International Journal of Coal Geology*, 38(3-4), pp. 237-260.

Cherubini, F. (2010). The biorefinery concept: Using biomass instead of oil for producing energy and chemicals. *Energy Conversion and Management*, 51(7), pp. 1412-1421.

Claisse, F. & Quintin, M. (1967). Generalization of the Lachance-Traill method for the correction of the matrix effect in X-ray fluorescence analysis. *Can Spectrosc*, 12, pp. 129-134.

Clark, D.H., Mayland, H.F. & Lamb, R.C. (1987). Mineral Analysis of Forages with near Infrared Reflectance Spectroscopy. *Agron. J.*, 79(3), pp. 485-490.

Cody, G.D., Brandes, J., Jacobsen, C. & Wirick, S. (2009). Soft X-ray induced chemical modification of polysaccharides in vascular plant cell walls. *Journal of Electron Spectroscopy and Related Phenomena*, 170(1–3), pp. 57-64.

Coppens, P., Cox, D., Vlieg, E. & Robinson, I.K. (1992). Synchrotron radiation crystallography. *London, Academic Press.*

Corma, A., Iborra, S. & Velty, A. (2007). Chemical routes for the transformation of biomass into chemicals. *Chemical Reviews*, 107(6), pp. 2411-2502.

Cox, P.M., Betts, R.A., Jones, C.D., Spall, S.A. & Totterdell, I.J. (2000). Acceleration of global warming due to carbon-cycle feedbacks in a coupled climate model. *Nature*, 408(6809), pp. 184-187.

Criss, J.W. & Birks, L.S. (1968). Calculation methods for flourescent X-ray spectrometry - empirical coefficients vs fundamental parameters. *Analytical Chemistry*, 40(7), pp. 1080-&.

Criss, J.W., Birks, L.S. & Gilfrich, J.V. (1978). Versatile X-ray analysis program combining fundamental parameters and empirical coefficients. *Analytical Chemistry*, 50(1), pp. 33-37.

Daszykowski, M., Kaczmarek, K., Heyden, Y.V. & Walczak, B. (2007). Robust statistics in data analysis - A review basic concepts. *Chemometrics and Intelligent Laboratory Systems*, 85(2), pp. 203-219.

Davidsson, K.O., Amand, L.E., Steenari, B.M., Elled, A.L., Eskilsson, D. & Leckner, B. (2008). Countermeasures against alkali-related problems during combustion of biomass in a circulating fluidized bed boiler. *Chemical Engineering Science*, 63(21), pp. 5314-5329.

Davies, T. (1998). The history of near infrared spectroscopic analysis: Past, present and future "From sleeping technique to the morning star of spectroscopy". *Analusis*, 26(4), pp. 17-19.

Dejong, S. (1993). SIMPLS - an alternative approach to partial least-squares regression. *Chemometrics and Intelligent Laboratory Systems*, 18(3), pp. 251-263.

di Stasio, S. & Braun, A. (2005). Comparative NEXAFS Study on Soot Obtained from an Ethylene/Air Flame, a Diesel Engine, and Graphite. *Energy & Fuels*, 20(1), pp. 187-194.

Dunisch, O., Richter, H.G. & Koch, G. (2010). Wood properties of juvenile and mature heartwood in Robinia pseudoacacia L. *Wood Science and Technology*, 44(2), pp. 301-313.

Ergon, R. (2002). PLS score-loading correspondence and a bi-orthogonal factorization. *Journal of Chemometrics*, 16(7), pp. 368-373.

Eriksson, L., Johansson, E. & Kettapeh-Wold, S. (1999). *Introduction to Multi- and Megavariate Data Analysis Using Projection Methods (PCA & PLS)*: Umetrics. Available from: http://books.google.se/books?id=3aW8GwAACAAJ.

Esbensen, K. & Geladi, P. (1989). Strategy of multivariate image-analysis (MIA). *Chemometrics and Intelligent Laboratory Systems*, 7(1-2), pp. 67-86.

Esteban, L.G., Gasson, P., Climent, J.M., de Palacios, P. & Guindeo, A. (2005). The wood of Pinus canariensis and its resinous heartwood. *Iawa Journal*, 26(1), pp. 69-77.

Fantazzini, D., Höök, M. & Angelantoni, A. (2011). Global oil risks in the early 21st century. *Energy Policy*, 39(12), pp. 7865-7873.

Francis, J.T. & Hitchcock, A.P. (1992). Inner-shell spectroscopy of p-benzoquinone, hydroquinone, and phenol: Distinguishing quinoid and benzenoid structures. *Journal of Physical Chemistry*, 96(16), pp. 6598-6610.

Geladi, P., MacDougall, D. & Martens, H. (1985). Linearization and Scatter-Correction for Near-Infrared Reflectance Spectra of Meat. *Applied Spectroscopy*, 39(3), pp. 491-500.

Geladi, P., Wold, S. & Esbensen, K. (1986). Image-analysis and chemical informations in images. *Analytica Chimica Acta*, 191, pp. 473-480.

Gilliham, M., Dayod, M., Hocking, B.J., Xu, B., Conn, S.J., Kaiser, B.N., Leigh, R.A. & Tyerman, S.D. (2011). Calcium delivery and storage in plant leaves: exploring the link with water flow. *Journal of Experimental Botany*, 62(7), pp. 2233-2250.

Golub, G.H. & Reinsch, C. (1970). Singular value decomposition and least squares solutions. *Numerische Mathematik*, 14(5), pp. 403-&.

Grunes, L.A. (1983). Study of the K edges of 3d transition-metals in pure and oxide form by X-ray-absorption spectroscopy. *Physical Review B*, 27(4), pp. 2111-2131.

Haro, P., Ollero, P., Perales, A.L.V. & Vidal-Barrero, F. (2013). Potential routes for thermochemical biorefineries. *Biofuels Bioproducts & Biorefining-Biofpr*, 7(5), pp. 551-572.

Hernandez, J.J., Aranda-Almansa, G. & Bula, A. (2010). Gasification of biomass wastes in an entrained flow gasifier: Effect of the particle size and the residence time. *Fuel Processing Technology*, 91(6), pp. 681-692.

Himmel, M.E., Ding, S.-Y., Johnson, D.K., Adney, W.S., Nimlos, M.R., Brady, J.W. & Foust, T.D. (2007). Biomass Recalcitrance: Engineering Plants and Enzymes for Biofuels Production. *Science*, 315(5813), pp. 804-807.

Hirsch, R.L. (2008). Mitigation of maximum world oil production: Shortage scenarios. *Energy Policy*, 36(2), pp. 881-889.

Huang, C., Han, L., Yang, Z. & Liu, X. (2009). Exploring the use of near infrared reflectance spectroscopy to predict minerals in straw. *Fuel*, 88(1), pp. 163-168.

IEA (2013). Key World Energy Statistics 2013. *Paris, France*.

IPCC (2013). Summary for Policymakers In: Climate Change 2013: The Physical Science Basis. Contribution of Working Group I to the fifth Assessment Report of the Intergovernmental Panel on Climate Change.([Stocker, T.F., D. Qin, G.-K. Plattner, M. Tignor, S.K. Allen, J. Boschung, A. Nauels, Y. Xia, V. Bex and P.M. Midgley (eds.)].), pp. Cambridge University Press, Cambridge, United Kingdom and New York, NY, USA.

Jenkins, B.M., Baxter, L.L., Miles Jr, T.R. & Miles, T.R. (1998). Combustion properties of biomass. *Fuel Processing Technology*, 54(1–3), pp. 17-46.

Jenkins, R. (1999). X-Ray Fluorescence Spectrometry. In: *X-Ray Fluorescence Spectrometry* John Wiley & Sons, Inc., pp. i-xix. Available from: http://dx.doi.org/10.1002/9781118521014.fmatter.

Johnson, E. (2009). Goodbye to carbon neutral: Getting biomass footprints right. *Environmental Impact Assessment Review*, 29(3), pp. 165-168.

Jolliffe, I.T. (1986). Principal Component Analysis, SpringerVerlag(Berlin, Germany).

Kaffka, K.J., Norris, K.H. & Roszakiss, M. (1982). Determining fat, protein and water-content of pastry products by the NIR technique. *Acta Alimentaria*, 11(2), pp. 199-217.

Kamm, B. & Kamm, M. (2004). Principles of biorefineries. *Applied Microbiology and Biotechnology*, 64(2), pp. 137-145.

Kassman, H., Pettersson, J., Steenari, B.M. & Amand, L.E. (2013). Two strategies to reduce gaseous KCl and chlorine in deposits during biomass combustion - injection of ammonium sulphate and co-combustion with peat. *Fuel Processing Technology*, 105, pp. 170-180.

Kenney, K.L., Smith, W.A., Gresham, G.L. & Westover, T.L. (2012). Understanding biomass feedstock variability. *Biofuels*, 4(1), pp. 111-127.

Krause, M.O. (1979). Atomic radiative and radiationless yields for K-shells and L-shells. *Journal of Physical and Chemical Reference Data*, 8(2), pp. 307-327.

Kumar, A., Jones, D.D. & Hanna, M.A. (2009). Thermochemical Biomass Gasification: A Review of the Current Status of the Technology. *Energies*, 2(3), pp. 556-581.

Lachance, G.R. & Claisse, F. (1980). A comprehensive alpha coefficient algorithm. *Adv. X-ray Anal.*, 23, pp. 87-92.

Lachance, G.R. & Traill, R.J. (1966). A practical solution to the matrix problem in X-ray analysis. *Can Spectrosc*, 11, pp. 43-48.

Lerotic, M., Jacobsen, C., Schäfer, T. & Vogt, S. (2004). Cluster analysis of soft X-ray spectromicroscopy data. *Ultramicroscopy*, 100(1–2), pp. 35-57.

Lestander, T.A., Finell, M., Samuelsson, R., Arshadi, M. & Thyrel, M. (2012). Industrial scale biofuel pellet production from blends of unbarked softwood and hardwood stems-the effects of raw material composition and moisture content on pellet quality. *Fuel Processing Technology*, 95, pp. 73-77.

Lestander, T.A., Johnsson, B. & Grothage, M. (2009). NIR techniques create added values for the pellet and biofuel industry. *Bioresource Technology*, 100(4), pp. 1589-1594.

Lestander, T.A. & Rhen, C. (2005). Multivariate NIR spectroscopy models for moisture, ash and calorific content in biofuels using bi-orthogonal partial least squares regression. *Analyst*, 130(8), pp. 1182-1189.

Lestander, T.A. & Samuelsson, R. (2010). Prediction of Resin and Fatty Acid Content of Biorefinery Feedstock by On-line Near-Infrared (NIR) Spectroscopy. *Energy & Fuels*, 24, pp. 5148-5152.

Lindstrom, E., Sandstrom, M., Bostrom, D. & Ohman, M. (2007). Slagging characteristics during combustion of cereal grains rich in phosphorus. *Energy & Fuels*, 21(2), pp. 710-717.

Martens, H. & Jensen, S.-Å. (1983). Partial Least Squares regression_ a new two-stage NIR calibration metod. *Progress in Cereal Chemistry and Technology*, pp. Elsevier, Amsterdam. p607-647.

Martens, H. & Næs, T. (1987). Multivariate calibration by data compression. *In: Near-infrared technology in agricultural and food industries*, pp. American Association of Cereal Chemists, St. Paul,Minnesota, USA. p 57-87.

Martens, H. & Næs, T. (1989). Multivariate Calibration, pp. John Wiley & Son, Chichester, UK.

Mohan, D., Pittman, C.U. & Steele, P.H. (2006). Pyrolysis of Wood/Biomass for Bio-oil: A Critical Review. *Energy & Fuels*, 20(3), pp. 848-889.

Moseley, H.G.J. (1913). XCIII. The high-frequency spectra of the elements. *Philosophical Magazine Series 6*, 26(156), pp. 1024-1034.

Navrotsky, A., Putnam, R.L., Winbo, C. & Rosen, E. (1997). Thermochemistry of double carbonates in the K2CO3-CaCO3 system. *American Mineralogist*, 82(5-6), pp. 546-548.

Newville, M. (2004). Fundamentals of XAFS. *xafs.org*.

Ng, K.L., Chadwick, D. & Toseland, B.A. (1999). Kinetics and modelling of dimethyl ether synthesis from synthesis gas. *Chemical Engineering Science*, 54(15-16), pp. 3587-3592.

NOAA (2013). pp. U.S. Departement of Commerce, National Oceanic & Atmospheric Administration, Earth System Research Laboratory, Boulder, Co. (accessed 25.09.14) http://www.esrl.noaa.gov/gmd/ccgg/trends/mlo.html#mlo.

Norgaard, L., Saudland, A., Wagner, J., Nielsen, J.P., Munck, L. & Engelsen, S.B. (2000). Interval partial least-squares regression (iPLS): A comparative chemometric study with an example from near-infrared spectroscopy. *Applied Spectroscopy*, 54(3), pp. 413-419.

Norris, K.H. (1992). *POSSIBLE MEDICAL APPLICATIONS OF NIR*. (Making Light Work : Advances in near Infrared Spectroscopy. Available from: <Go to ISI>://WOS:A1992BW33V00091.

Obernberger, I. & Thek, G. (2004). Physical characterisation and chemical composition of densified biomass fuels with regard to their combustion behaviour. *Biomass and Bioenergy*, 27(6), pp. 653-669.

Ohman, M., Nordin, A., Skrifvars, B.J., Backman, R. & Hupa, M. (2000). Bed agglomeration characteristics during fluidized bed combustion of biomass fuels. *Energy & Fuels*, 14(1), pp. 169-178.

Pearson, K. (1901). On lines and planes of closest fit to systems of points in space. *Philosophical Magazine*, Series 6, vol. 2(11), pp. 559-572.

Pereira, F.M.V., Pereira, E.R. & Bueno, M. (2006). Development of a methodology for calcium, iron, potassium, magnesium, manganese, and zinc quantification in teas using X-ray spectroscopy and multivariate calibration. *Journal of Agricultural and Food Chemistry*, 54(16), pp. 5723-5730.

Phanphanich, M. & Mani, S. (2011). Impact of torrefaction on the grindability and fuel characteristics of forest biomass. *Bioresource Technology*, 102(2), pp. 1246-1253.

Prins, M.J., Ptasinski, K.J. & Janssen, F.J.J.G. (2006). Torrefaction of wood. Part 1. Weight loss kinetics. *Journal of Analytical and Applied Pyrolysis*, 77(1), pp. 28-34.

Ragauskas, A.J., Williams, C.K., Davison, B.H., Britovsek, G., Cairney, J., Eckert, C.A., Frederick, W.J., Hallett, J.P., Leak, D.J., Liotta, C.L., Mielenz, J.R., Murphy, R., Templer, R. & Tschaplinski, T. (2006). The path forward for biofuels and biomaterials. *Science*, 311(5760), pp. 484-489.

Rasberry, S.D. & Heinrich, K.F. (1974). Calibration for interelement effects in X-ray-flourescence analysis. *Analytical Chemistry*, 46(1), pp. 81-89.

Ravel, B. & Newville, M. (2005). ATHENA, ARTEMIS, HEPHAESTUS: data analysis for X-ray absorption spectroscopy using IFEFFIT. *Journal of Synchrotron Radiation*, 12, pp. 537-541.

Rehr, J.J., Ankudinov, A. & Zabinsky, S.I. (1998). New developments in NEXAFS/EXAFS theory. *Catalysis Today*, 39(4), pp. 263-269.

Rehr, J.J., Deleon, J.M., Zabinsky, S.I. & Albers, R.C. (1991). Theoretical X-ray absorption fine-structure standards. *Journal of the American Chemical Society*, 113(14), pp. 5135-5140.

Reich, G. (2005). Near-infrared spectroscopy and imaging: Basic principles and pharmaceutical applications. *Advanced Drug Delivery Reviews*, 57(8), pp. 1109-1143.

Roine, A. (2006). HSC Chemistry 6.12, p. Outotec Tesearch Oy.

Rousseau, R.M. (1984). Fundamental algorithm between concentration and intensity in XRF analysis .1. Theory. *X-Ray Spectrometry*, 13(3), pp. 115-120.

Saeys, W., Mouazen, A.M. & Ramon, H. (2005). Potential for onsite and online analysis of pig manure using visible and near infrared reflectance spectroscopy. *Biosystems Engineering*, 91(4), pp. 393-402.

Samuelsson, R., Burvall, J. & Igsell, P. (1995). Report on Round Robin Analysis of Peat and Biofuels, pp. Swedish University of Agricultural Sciences, Department of Agricultural Research for Northern Sweden, Umeå, Sweden.

Sanchez, O.J. & Cardona, C.A. (2008). Trends in biotechnological production of fuel ethanol from different feedstocks. *Bioresource Technology*, 99(13), pp. 5270-5295.

Savitzky, A. & Golay, M.J.E. (1964). Smoothing and Differentiation of Data by Simplified Least Squares Procedures. *Analytical Chemistry*, 36(8), pp. 1627-1639.

Schneider, A. (1901). The Probable Function of Calcium Oxalate Crystals in Plants. *Botanical Gazette*, 32(2), pp. 142-144.

Schneider, C.A., Rasband, W.S. & Eliceiri, K.W. (2012). NIH Image to ImageJ: 25 years of image analysis. *Nature Methods*, 9(7), pp. 671-675.

Sheppard, N., Willis, H.A. & Rigg, J.C. (1985). Names, Symbols, Definitions and units of quantities in optical spectroscopy. *Pure and Applied Chemistry*, 57(1), pp. 105-120.

Sherman, J. (1955). The theoretical derivation of fluorescent X-ray intensities from mixtures. *Spectrochimica Acta*, 7(5), pp. 283-306.

Shoulaifar, T.K., DeMartini, N., Zevenhoven, M., Verhoeff, F., Kiel, J. & Hupa, M. (2013). Ash-Forming Matter in Torrefied Birch Wood: Changes in Chemical Association. *Energy & Fuels*, 27(10), pp. 5684-5690.

Sun, R.C., Tomkinson, J., Wang, Y.X. & Xiao, B. (2000). Physico-chemical and structural characterization of hemicelluloses from wheat straw by alkaline peroxide extraction. *Polymer*, 41(7), pp. 2647-2656.

Swerts, J., Vanespen, P. & Geladi, P. (1993). Partial Least-Squares techniques in the energy-dispersive X-ray-fluprescence determinations of sulfur graphite mixtures. *Analytical Chemistry*, 65(9), pp. 1181-1185.

Takamasa, A. & Nakai, S. (2009). Contamination introduced during rock sample powdering: Effects from different mill materials on trace element contamination. *Geochemical Journal*, 43(5), pp. 389-394.

Tao, G.C., Lestander, T.A., Geladi, P. & Xiong, S.J. (2012). Biomass properties in association with plant species and assortments I: A synthesis based on literature data of energy properties. *Renewable & Sustainable Energy Reviews*, 16(5), pp. 3481-3506.

Thompson, G. & Bankston, D.C. (1970). Sample Contamination from Grinding and Sieving Determined by Emission Spectrometry. *Applied Spectroscopy*, 24(2), pp. 210-219.

Tijmensen, M.J.A., Faaij, A.P.C., Hamelinck, C.N. & van Hardeveld, M.R.M. (2002). Exploration of the possibilities for production of Fischer Tropsch liquids and power via biomass gasification. *Biomass & Bioenergy*, 23(2), pp. 129-152.

Trygg, J. & Wold, S. (2002). Orthogonal projections to latent structures (O-PLS). *Journal of Chemometrics*, 16(3), pp. 119-128.

Umbach, F. (2010). Global energy security and the implications for the EU. *Energy Policy*, 38(3), pp. 1229-1240.

UN (2012). World Population Prospects, The 2012 Revision(New York, USA).

UN (2014). Population and Vital Statistics Report. *Statistical Papers, Series A*, LXVI, pp. New York, USA.

van der Stelt, M.J.C., Gerhauser, H., Kiel, J.H.A. & Ptasinski, K.J. (2011). Biomass upgrading by torrefaction for the production of biofuels: A review. *Biomass & Bioenergy*, 35(9), pp. 3748-3762.

Wang, L., Weller, C.L., Jones, D.D. & Hanna, M.A. (2008). Contemporary issues in thermal gasification of biomass and its application to electricity and fuel production. *Biomass and Bioenergy*, 32(7), pp. 573-581.

Vassilev, S.V., Baxter, D., Andersen, L.K. & Vassileva, C.G. (2010). An overview of the chemical composition of biomass. *Fuel*, 89(5), pp. 913-933.

Vassilev, S.V., Baxter, D., Andersen, L.K. & Vassileva, C.G. (2013a). An overview of the composition and application of biomass ash. Part 1. Phase-mineral and chemical composition and classification. *Fuel*, 105, pp. 40-76.

Vassilev, S.V., Baxter, D., Andersen, L.K., Vassileva, C.G. & Morgan, T.J. (2012). An overview of the organic and inorganic phase composition of biomass. *Fuel*, 94(1), pp. 1-33.

Vassilev, S.V., Baxter, D. & Vassileva, C.G. (2013b). An overview of the behaviour of biomass during combustion: Part I. Phase-mineral transformations of organic and inorganic matter. *Fuel*, 112(0), pp. 391-449.

Weng, J.K., Li X Fau - Bonawitz, N.D., Bonawitz Nd Fau - Chapple, C. & Chapple, C. (2008). Emerging strategies of lignin engineering and degradation for cellulosic biofuel production(0958-1669 (Print)).

Werkelin, J., Skrifvars, B.J. & Hupa, M. (2005). Ash-forming elements in four Scandinavian wood species. Part 1: Summer harvest. *Biomass & Bioenergy*, 29(6), pp. 451-466.

Werther, J., Saenger, M., Hartge, E.U., Ogada, T. & Siagi, Z. (2000). Combustion of agricultural residues. *Progress in Energy and Combustion Science*, 26(1), pp. 1-27.

Westad, F., Schmidt, A. & Kermit, M. (2008). Incorporating chemical band-assignment in near infrared spectroscopy regression models. *Journal of near Infrared Spectroscopy*, 16(3), pp. 265-273.

Williams, G.P. (2009). X-ray properties of the elements(Section 1.1). *In X-ray Data Booklet.*, Lawrence Berkeley National Laboratory, Center for X-ray Optics and Advanced Light Source, LBLN/Pub-490 Rev. 3.

Williams, P. & Sobering, D. (1993). Comparison of commercial near infrared transmittance and reflectance instruments for analysis of whole grains and seeds. *Journal of near Infrared Spectroscopy*, 1(1), p. 25.

Wold, H. (1966). Nonlinear estimation by iterative least squares procedures, Ed Wiley, p. New York.

Wold, H. (1975). Path modelswith latent variables: the NIPALS approach. *In: Quantitative Sociology*, pp. Academic Press, New York, USA. p 305-357.

Wold, S. (1994). PLS for Multivariate Linear Modeling. *QSAR; Chemometric Mehods in Molecular Design. Methods and Principels in Medicinal Chemistry*, p. Ed. Wiley.

Wold, S., Albano, C., Dunn, W.J., III, Edlund, U., Esbensen, K., Geladi, P., Hellberg, S., Johansson, E., Lindberg, W. & Sjöström, M. (1984). Multivariate Data Analysis in Chemistry. In: Kowalski, B. (ed. *Chemometrics*. (NATO ASI Series, 138) Springer Netherlands, pp. 17-95. Available from: http://dx.doi.org/10.1007/978-94-017-1026-8_2.

Wold, S., Antti, H., Lindgren, F. & Ohman, J. (1998). Orthogonal signal correction of near-infrared spectra. *Chemometrics and Intelligent Laboratory Systems*, 44(1-2), pp. 175-185.

Wold, S., Esbensen, K. & Geladi, P. (1987). Principal component analysis. *Chemometrics and Intelligent Laboratory Systems*, 2(1-3), pp. 37-52.

Wu, H., Pedersen, A.J., Glarborg, P., Frandsen, F.J., Dam-Johansen, K. & Sander, B. (2011). Formation of fine particles in co-combustion of coal and solid recovered fuel in a pulverized coal-fired power station. *Proceedings of the Combustion Institute*, 33, pp. 2845-2852.

Xiao, B., Sun, X.F. & Sun, R. (2001). Chemical, structural, and thermal characterizations of alkali-soluble lignins and hemicelluloses, and cellulose from maize stems, rye straw, and rice straw. *Polymer Degradation and Stability*, 74(2), pp. 307-319.

Xiong, S.J., Burvall, J., Orberg, H., Kalen, G., Thyrel, M., Ohman, M. & Bostrom, D. (2008). Slagging characteristics during combustion of corn stovers with and without kaolin and calcite. *Energy & Fuels*, 22(5), pp. 3465-3470.

Xiong, S.J., Landstrom, S. & Olsson, R. (2009). Delayed harvest of reed canary grass translocates more nutrients in rhizomes. *Acta Agriculturae Scandinavica Section B-Soil and Plant Science*, 59(4), pp. 306-316.

Yaman, S. (2004). Pyrolysis of biomass to produce fuels and chemical feedstocks. *Energy Conversion and Management*, 45(5), pp. 651-671.

Zhao, M. & Running, S.W. (2010). Drought-Induced Reduction in Global Terrestrial Net Primary Production from 2000 Through 2009. *Science*, 329(5994), pp. 940-943.